Received: 31 December 2014 | Revised: 2 November 2015 | Published on: 3 April 2017

DOI: 10.1002/asna.201712978

ORIGINAL ARTICLE

Astronomische Nachrichten

A dynamical evolution study of 40 2MASS open clusters

Orhan Güneş[1,2*] | **Yüksel Karataş**[2] | **Charles Bonatto**[3]

[1]Faculty of Arts and Humanities, Department of History of Science, Istanbul Medeniyet University, Istanbul, Turkey
[2]Science Faculty, Department of Astronomy and Space Sciences, Istanbul University, Istanbul, Turkey
[3]Departamento de Astronomia, Universidade Federal do Rio Grande do Sul, Porto Alegre, Brazil

***Correspondence**
Orhan Günes, Faculty of Arts and Humanities, Department of History of Science, Istanbul Medeniyet University, Kadikoy, Istanbul, Turkey.
Email: or.gunes@gmail.com

Funding Information
This research was supported by the National Aeronautics and Space Administration, National Science Foundation,

We investigate the dynamical evolution of 40 open clusters (OCs) by means of their astrophysical parameters derived from field-decontaminated 2MASS photometry. We find a bifurcation in the planes' core radius versus age and cluster radius versus age, in which part of the clusters appear to expand with time probably due to the presence of stellar black holes while others seem to shrink due to dynamical relaxation. Mass functions (MFs) are built for three-fourth of the sample (31 OCs), which are used to search for indications of mass segregation and external dynamical processes by means of relations between astrophysical, structural, and evolutionary parameters. We detect a flattening of MF slopes occurring at the evolutionary parameters $\tau_{\rm core} \leq 32$ and $\tau_{\rm overall} \leq 30$, respectively.
Within the uncertainties involved, the overall MF slopes of 14 out of 31 OCs with $m_{\rm overall} > 500\,M_{\odot}$ are consistent with Kroupa's initial mass function, implying little, or no dynamical evolution for these clusters. The remaining 17 OCs with MF slopes departing from that of Kroupa show mild/large-scale mass segregation due to dynamical evolution.

KEYWORDS
CCD 2 MASS photometry – open clusters and associations – stars

1 | INTRODUCTION

The internal dynamical processes of open clusters (OCs) are mass loss during stellar evolution, mass segregation, and evaporation of its stellar content with time. Tidal interactions with the galaxy's disk and bulge, as well as collisions with giant molecular clouds (hereafter GMCs) are the main external dynamical effects upon OCs. Because of these dynamical interactions, as clusters age, their structures are subject to considerable changes, and may even be dissolved in the galactic field. A massive cluster can be dissolved by central tidal effects in ≈50 Myr (Bergond et al. 2001; Portegies Zwart et al. 2002). This time is much shorter than ∼1 Gyr found for most OCs within the solar circle (Bonatto & Bica 2006). Interactions with the galactic disk, the tidal pull of the galactic bulge, and collisions with GMCs destroy more easily the poorly populated OCs on a timescale of 10^8 year, particularly inside the solar circle (Bergond et al. 2001).

A cluster loses low-mass stars from its outer regions into the field by stellar evaporation. As a result of this mass segregation, low-mass stars are transferred from the cluster's core to its outskirts, while massive stars accumulate in the core (Bonatto & Bica 2005; Schilbach et al. 2006). This results in a flat mass function (hereafter MF) in the core and steep one in the halo. These external and internal dynamical processes play different roles, depending on the location of an OC with respect to the solar circle: old OCs with age > 1 Gyr tend to be concentrated in the anticenter, a region with a low density of GMCs (Camargo et al. 2009; van den Bergh & McClure 1980). Tidal shocks from the galaxy and from GMCs and observational incompleteness or biases are responsible for the scarcity of OCs in direction to the galactic center (Bonatto & Bica 2007a). Because of absorption and crowding in regions dominated by disk and bulge stars, the OCs' observational completeness is decreased. With the effect of tidal interaction, an OC heats and its stars gain kinetic energy, which leads to an increase in the evaporation rate.

In this paper we have considered 40 OCs with 2MASS JHK_s photometric data, which are selected in with respect to the cluster's location and the age (age ≥ 100 Myr) from the WEBDA OC and Dias et al. catalogs (Dias et al. 2012; Mermilliod 1992). These OCs have been considered to study their dynamical evolution, particularly in dependence of their location in the galaxy. We state that our sample is relatively small but our work have the advantage of being based on a uniform database, in the sense that we determine the parameters following the same methods, based on the same kind of photometry. The robust structural parameters have been derived from high-contrast stellar radial density profiles (RDPs) following the method of Bonatto & Bica (2007a), and the ages were derived from a fit of isochrones to decontaminated color-magnitude diagrams (CMDs) of the 2MASS JHK_s photometric data. As can be seen from the WEBDA database, charge-coupled device (CCD)-based CMDs of these 40 OCs are also available. We stress that the CMDs presented here go fainter than is available there.

From our sample of young, intermediate, and old OCs (age between 100 Myr and 5 Gyr), the relations between the dynamical evolution indicators and cluster radius ($R_{\rm RDP}$, hereafter), core radius ($R_{\rm core}$, hereafter), mass, mass function slope χ, mass density ρ, evolutionary parameter τ, and the parameters (age, d, $R_{\rm GC}$, z) have been derived and compared with the values given in the literature. Here, d, $R_{\rm GC}$, and z denote heliocentric, galactocentric (hereafter $R_{\rm GC}$), and galactic plane distances, respectively. Such relations have been studied by Lynga (1982); Janes & Phelps (1994); Nilakshi et al. (2002); Tadross et al. (2002); Bonatto & Bica (2005); Schilbach et al. (2006); Sharma et al. (2006); Bonatto & Bica (2007a); Maciejewski & Niedzielski (2007); Bukowiecki et al. (2011), and Camargo et al. (2009). In this paper, $R_{\odot} = 7.2 \pm 0.3$ kpc, which is based on the updated distances of galactic globular clusters (Bica et al. 2006a).

The rest of the paper is organized as follows. The selection of the OCs is presented in Section 2. In Section 3, the 2MASS JHK_s photometry and the field star decontamination algorithm (employed in the CMD analyses) are given. The derivations of astrophysical and structural parameters, mass and mass functions, relaxation time, and evolutionary parameter are presented in Sections 4, 5, 6. Section 7 is devoted to results, which contain the following subsections: Section 7.1 the relation between $R_{\rm RDP}$ and $R_{\rm core}$, Section 7.2 the relations of cluster dimensions with distance and age, Section 7.3 the relations between $R_{\rm RDP}$ and age and $R_{\rm core}$ with age, Section 7.4 the relations $R_{\rm RDP}$ with $R_{\rm GC}$ and $R_{\rm core}$ with $R_{\rm GC}$, Section 7.5 the spatial distribution of the 40 OCs in the galaxy, Section 7.6 relations between the overall mass with ($R_{\rm RDP}$, $R_{\rm core}$) and with (age, $R_{\rm GC}$), Section 7.7 the relations between the mass density with MF slopes, age, $R_{\rm RDP}$ and with $R_{\rm GC}$, and Section 7.8 the relation between the MF slopes and the evolutionary parameter, and a comparison with Kroupa's IMF. Conclusions are presented in Section 8.

2 | OC SAMPLE AND SPATIAL DISTRIBUTION

We applied two criteria to select the OCs for our work from the WEBDA OC and Dias et al. catalogs (Dias et al. 2012; Mermilliod 1992). Namely, the cluster location in the galaxy and their ages, see Figure 1. In order to study dynamical evolution of middle and older age OCs, 40 OCs with age between 100 Myr and 5 Gyr as a function of the galactic location (see Figure 1, slices I–IV) from the 2MASS data base are considered. The location criterion is important because the longevity/survival rate of the OCs is related to the galactic slices inside/outside the solar circle. Over 40 OCs in the WEBDA OC Mermilliod (1992) and Dias et al. (2012) catalog have been considered. The OCs that were not appropriate to the decontamination technique of field stars were eliminated by examining their decontamination surface density distributions (Section 3). Thus the sample size became 40 OCs. We are aware that the sample is not large, but we concluded that the sample with robust parameters would be significant to address the dynamical problems mentioned earlier. From the 40 OCs, we have also studied the relations between the parameters (age, d, $R_{\rm GC}$, z) and dynamical indicators ($R_{\rm core}$, $R_{\rm RDP}$, m, χ, τ).

A total of 1,148 OCs out of 2,000 OCs in the Dias et al. (2012) catalog, which can be considered the most representative for our purpose, have age determinations. As can be seen from Table 1, there are 13 OCs with age between 200 Myr and 1 Gyr (3.5%), 26 OCs with age between 1 Gyr and 5 Gyr (14.5%), and one with age ≤200 Myr in our sample.

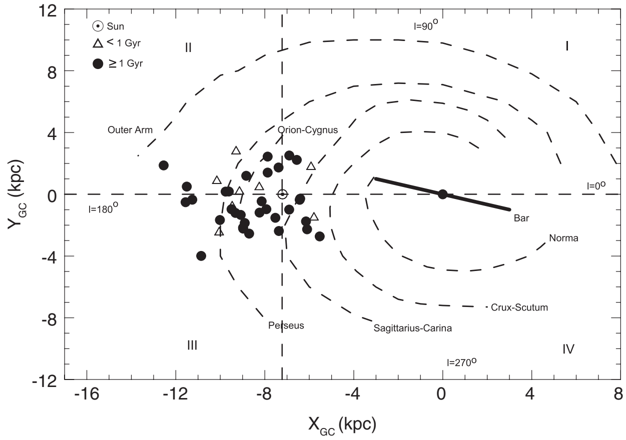

FIGURE 1 Spatial distribution (X,Y) of 40 OCs. Open triangles and filled circles represent OCs with ages younger than 1 Gyr and older than 1 Gyr, respectively. The schematic projection of the galaxy is seen from the North Pole. The sun's distance to the galactic center is taken to be 7.2 kpc of Bica et al. (2006a)

TABLE 1 Comparison of our cluster sample to the catalogue of Dias et al. (2012) for the age data

Age (Myr)	N (This work)	N (Dias)	Percentage (%)
Age < 200	1	579	0.17
200 ≤ Age < 1,000	13	373	3
1,000 ≤ Age < 5,000	26	179	15
5,000 ≤ Age ≤ 10,000	—	17	—
Total	40	1,148	3

The spatial distribution in the XY-plane together with the spiral arms[1] of the 40 OCs is displayed in Figure 1. As can be seen from the figure, our sample comprises the OCs of four galactic slices (I–IV). Note that the number of OCs toward the anticenter in Figure 1 is larger than the ones toward the galactic center directions. Six out of eight OCs with age < 1 Gyr fall in the galactic anticenter directions, whereas the remaining two occupy the galactic center direction. This is because the OCs in galactic center directions could not be observed because of strong absorption or crowding, or were systematically dissolved by different tidal effects such as high frequency of collisions with GMCs (Gieles et al. 2006).

The majority of OCs with age ≥ 1 Gyr lie outside the solar circle. From Figure 1, one readily sees that the number of OCs inside the solar radius is biased in the direction of the galactic center. The reason is that the inner galaxy clusters cannot be observed because of strong absorption and crowding, or because they have been dissolved by a combination of tidal effects. In good measure, the latter is caused by the expected higher frequency of collisions with GMCs in that direction (Camargo et al. 2009; Gieles et al. 2006). From an inspection of Figure 1, there are more OCs in the anticenter direction than in the opposite direction, in agreement with van den Bergh & McClure (1980), who find that the OCs with age ≥ 1 Gyr tend to be concentrated in the anticenter, which is a region with lower density of GMCs. Our sample has small statistics to draw significant conclusions in that respect. However, statistically, working with a representative subpopulation of the galactic OCs minimizes the occurrence of biases in the analyses.

Finally, to put the present OC sample in context, in Figure 2 we compare some observational data together with fundamental parameters (derived in subsequent sections) with the corresponding ones found in OC databases. This analysis is also important for checking for the presence of systematic biases in our sample. For this analysis, we use the parameters derived by Kharchenko et al. (2013) for 3,006 OCs. The advantage of their work is that the parameters follow from a systematic and uniform analysis. Since Kharchenko et al. (2013) do not provide cluster mass, we take such values from Piskunov et al. (2008), although for a smaller number of OCs (236).

Our analysis compares distribution functions of the several parameters between both sets, as is seen from Figure 2. Uncertainties in the parameters have been incorporated into the respective distribution function. And, since the sample differs significantly in the number of OCs, the distribution functions have been scaled to provide the best visual comparison between both. The top panels of Figure 2 show how the OCs distribute with respect to the galactic longitude (left) and latitude (right). Clearly, most of our sample

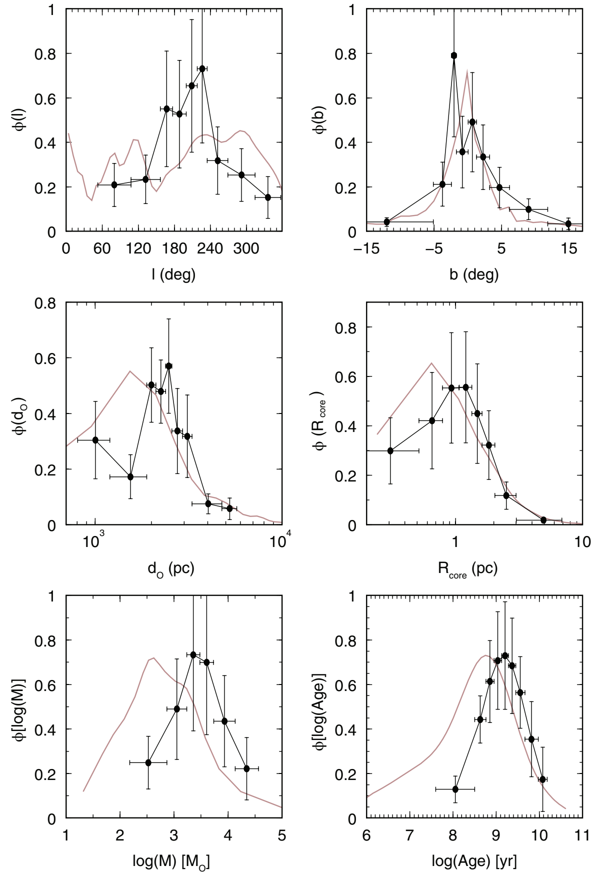

FIGURE 2 Normalized distribution functions of our OC sample (circles) compared to those of Kharchenko et al. (2013) and Piskunov et al. (2008) (solid line)

corresponds to clusters directed towards the second and third galactic quadrants. Regarding galactic latitude, our sample tends to avoid the plane. In terms of distance from the sun (middle-left), our sample is somewhat consistent with that of Kharchenko et al. (2013), particularly for distances >2 kpc. The same applies to the core radius (middle-right) for $R_{\rm core} > 1$ pc; below this threshold, our sample appears to contain a lower fraction of OCs than in Kharchenko et al. (2013). Regarding mass, both distributions have a similar shape but with a shift of ≈0.7 dex between the peaks, which suggests that our sample occupies the high-mass wing observed in the Piskunov et al. (2008) distribution. The age distributions also have similar shapes, with our sample consisting essentially of clusters older than 100 Myr. Thus, we can conclude that the 40 OCs considered here comprise a representative subsample of the galactic OC population with no systematic biases.

3 | THE 2MASS PHOTOMETRY AND THE FIELD-STAR DECONTAMINATION

We have used JHK_s photometry of 2MASS[2] to find the apparent cluster members of 40 OCs (Skrutskie et al. 2006). We

[1] (X, Y) is a right handed Cartesian coordinate system with the Sun at its center, with the X-axis pointing toward the galactic center and the Y-axis pointing in the disk rotation direction.

[2] The *Two Micron All Sky Survey Catalogue*, available at http://www.ipac.caltech.edu/2mass/releases/allsky/

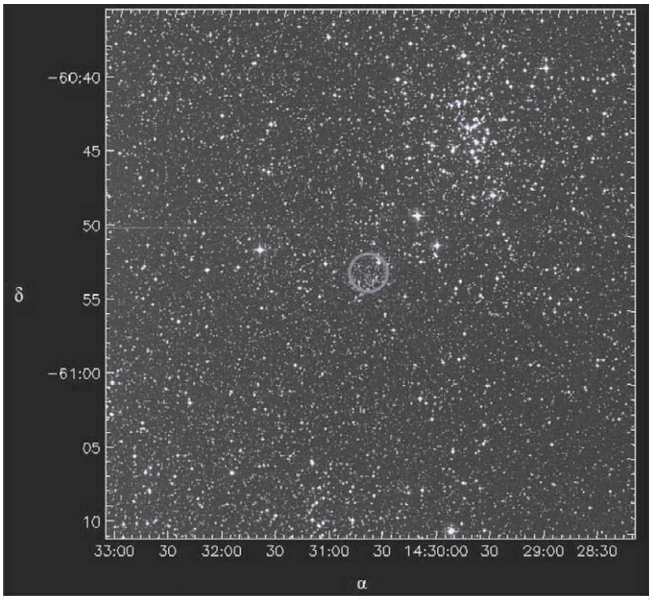

FIGURE 3 The image of Pismis 19 in DSS-I 25′ × 25′

used VizieR[3] to extract the near-infrared (NIR) (J, H, and K_s 2MASS) photometry for a large area centered on each cluster, which is essential to build the RDPs with a high contrast relative to the background and for a better field star decontamination. 2MASS provides an all-sky coverage with the spatial and photometric uniformity required for high star count statistics. For the photometric constraint, the 2MASS magnitude extractions have been restricted to stars with errors smaller than 0.2 mag in JHK_s magnitudes. The extraction radii of 40 OCs have been chosen by visual inspection on the DSS-I image,[4] and taking into account the RDP, in the sense that the profile must become relatively stable in the outer region. As an example, we show only the DSS-I image of Pismis 19 in Figure 3.

The technique used here for determining the cluster members of the 40 OCs is known as the field star decontamination procedure coupled to the 2MASS JHK_s photometry, which was successfully used by Bonatto & Bica (2007a, 2007b, 2008) and more recently by Güneş et al. (2012), This decontamination procedure was applied to the 40 OCs discussed here. This technique samples photometric properties of the stars in a neighboring comparison field considered free of cluster stars to (statistically) remove the contaminating field stars from the cluster stars with help of the CMDs.

First, the stellar surface densities σ (stars arcmin^{-2}) and the surface isopleths of both the raw and decontamination data of 40 OCs were computed for a mesh size of $3' \times 3'$ and centered on the galactic coordinates of Table 2. If necessary, we have redetermined them in this work (see below). Here, isopleth is the star density map. These maps have been used to maximize the contrast of the cluster against the background. In Figures 4 and 5, we show the result for Pismis 19 as an example. The central stellar density excesses are significant in the decontamination surface-density distributions, as is seen in Figure 5 for Pismis 19.

The stellar RDPs were derived from the isopleth surfaces of each cluster, the coordinates were checked, and the cluster radii were determined (Table 4). The residual background level of each RDP corresponds to the average number of CM-filtered stars measured in the comparison field. A wide external ring ($\Delta R = 13'$–$70'$) centered in the cluster (Col. 11 of Table 5) has been considered to eliminate field stars of the 40 OCs. Stars within the cluster radii have been considered to be probable members.

The stellar RDP of each cluster, built based on the JHK_s photometry extracted with the WEBDA[5] coordinates, are displayed in Table 2 and have been computed to check cluster centering. In some cases, the RDP built with the original cluster coordinates presented a dip at the center. Then, new central coordinates were searched after field star decontamination to maximize the star counts in the innermost RDP bin. From these RDPs, the cluster radii of 40 OCs were determined (Table 5). The stellar RDP is the projected number of stars per area around the cluster center. To avoid oversampling near the center and undersampling for large radii, the RDPs were built by counting stars in concentric rings of increasing width with distance to the center. The number and width of rings were optimized so that the resulting RDPs had adequate spatial resolution with moderate 1σ Poisson errors. The residual background level of each RDP corresponds to the average number of CM-filtered stars measured in the comparison field.

As Camargo et al. (2010) noted, RDPs of OCs built based on the WEBDA coordinates usually show a dip in the inner RDP region when a mismatch exists between the "true" and catalog coordinates. For this reason, new central coordinates of these clusters have been searched to maximize the star counts at the innermost RDP bin. Then, the 2MASS photometry was extracted again, but now centered on the optimized cluster coordinates. As a representative, the optimized central coordinate of Pismis 19 is displayed in Figure 3 as small circle, and given in the right section of Table 2.

To have the intrinsic morphology of the clusters in the CMD, as explained above, the statistical field star decontamination procedure of Bonatto & Bica (2007a) was used. This procedure is based on the relative star densities per sky area in a cluster region and on a neighboring offset field. It divides the full range of magnitudes and colors of a CMD into the cell dimensions of $\Delta(J) = 1.0$, and $\Delta(J-H) = \Delta(J-K_s) = 0.15$. These dimensions are adequate to allow for sufficient star counts in individual cells

[3]http://vizier.u-strasbg.fr/viz-bin/VizieR?-source$=$II/246
[4]Extracted from the Canadian Astronomy Data Center (CADC), at http://ledas-www.star.le.ac.uk/DSSimage/
[5]www.univie.ac.at/WEBDA (Mermilliod & Paunzen 2003)).

TABLE 2 Literature (left columns) and presently optimized (right columns) equatorial and galactic coordinates of 40 OCs

Cluster	α (2,000) (h m s)	δ (2,000) (° ′ ″)	l (°)	b (°)	α (2,000) (h m s)	δ (2,000) (° ′ ″)	l (°)	b (°)
NGC 436	01 15 58	58 48 42	126.11	−3.91	01 15 58	58 48 42	126.11	−3.91
King 5	03 14 45	52 41 12	143.78	−4.29	03 14 45	52 41 12	143.78	−4.29
NGC 1513	04 09 57	49 30 54	152.59	−1.57	04 09 50	49 31 17	152.57	−1.58
Be 15	05 02 06	44 30 43	162.26	1.62	05 02 06	44 30 43	162.26	1.62
NGC 1798	05 11 39	47 41 30	160.70	4.85	05 11 39	47 41 30	160.70	4.85
Be 17	05 20 36	30 36 00	175.65	−3.65	05 20 38	30 34 28	175.67	−3.66
NGC 1907	05 28 05	35 19 30	172.62	0.31	05 28 09	35 18 20	172.64	0.31
NGC 2112	05 53 45	00 24 36	205.87	−12.62	05 53 51	00 25 44	205.87	−12.58
Koposov 12	06 00 56	35 16 36	176.16	6.00	06 00 56	35 16 36	176.16	6.00
NGC 2158	06 07 25	24 05 48	186.63	1.78	06 07 30	24 05 50	186.64	1.80
Koposov 53	06 08 56	26 15 49	184.90	3.13	06 08 56	26 15 49	184.90	3.13
NGC 2194	06 13 45	12 48 24	197.25	−2.35	06 13 45	12 48 24	197.25	−2.35
NGC 2192	06 15 17	39 51 18	173.42	10.65	06 15 22	39 51 06	173.42	10.67
NGC 2243	06 29 34	−31 17 00	239.48	−18.01	06 29 34	−31 17 00	239.48	−18.01
Trumpler 5	06 36 42	09 26 00	202.86	1.05	06 36 36	09 25 21	202.86	1.02
Col 110	06 38 24	02 01 00	209.65	−1.98	06 38 35	02 01 30	209.66	−1.93
NGC 2262	06 39 38	01 08 36	210.57	−2.10	06 39 38	01 08 36	210.57	−2.10
NGC 2286	06 47 40	−03 08 54	215.31	−2.27	06 47 43	−03 10 20	215.33	−2.27
NGC 2309	06 56 03	−07 10 30	219.84	−2.24	06 56 02	−07 11 05	219.85	−2.25
Tombaugh 2	07 03 05	−20 49 00	232.83	−6.88	07 03 05	−20 49 00	232.83	−6.88
Be 36	07 16 06	−13 06 00	227.38	−0.59	07 16 24	−13 11 23	227.49	−0.56
Haffner 8	07 23 24	−12 20 00	227.53	1.34	07 23 09	−12 16 12	227.45	1.32
Mel 71	07 37 30	−12 04 00	228.95	4.50	07 37 30	−12 04 00	228.95	4.50
NGC 2425	07 38 22	−14 52 54	231.52	3.31	07 38 22	−14 52 54	231.52	3.31
NGC 2506	08 00 01	−10 46 12	230.56	9.93	07 59 59	−10 45 28	230.55	9.93
Pismis 3	08 31 22	−38 39 00	257.86	0.50	08 31 16	−38 39 02	257.85	0.48
NGC 2660	08 42 38	−47 12 00	265.93	−3.01	08 42 38	−47 12 00	265.93	−3.01
NGC 3680	11 25 38	−43 14 36	286.76	16.92	11 25 35	−43 15 11	286.76	16.91
Ru 96	11 50 38	−62 08 23	295.89	−0.10	11 50 37	−62 09 04	295.89	−0.11
Ru 105	12 34 15	−61 34 11	300.88	1.24	12 34 12	−61 33 00	300.88	1.25
Trumpler 20	12 39 34	−60 37 00	301.48	2.22	12 39 34	−60 37 00	301.48	2.22
Pismis 19	14 30 40	−60 53 00	314.71	−0.30	14 30 40	−60 53 00	314.71	−0.30
NGC 6134	16 27 46	−49 09 06	334.92	−0.20	16 27 46	−49 09 06	334.92	−0.20
IC 4651	17 24 49	−49 56 00	340.09	−7.91	17 24 46	−49 55 06	340.10	−7.89
NGC 6802	19 30 35	20 15 42	55.33	0.92	19 30 33	20 15 48	55.32	0.92
NGC 6819	19 41 18	40 11 12	73.98	8.48	19 41 18	40 11 12	73.98	8.48
Be 89	20 24 36	46 03 00	83.16	4.82	20 24 30	46 02 53	83.15	4.84
NGC 6939	20 31 30	60 39 42	95.90	12.30	20 31 30	60 39 42	95.90	12.30
NGC 7142	21 45 09	65 46 30	105.35	9.48	21 45 12	65 47 43	105.36	9.50
NGC 7789	23 57 24	56 42 30	115.53	−5.39	23 57 24	56 42 30	115.53	−5.39

and preserve the intrinsic morphology of the evolutionary sequences. Bonatto & Bica (2007a) showed that the field star decontamination procedure with 2MASS JHK_s photometry is efficient in isolating those stars with a high probability of being cluster members. More details on the algorithm can be found in Bonatto & Bica (2007a, 2007b); Bonatto & Bica (2009a, 2009b, 2009c), and (Camargo et al. 2010).

By following the field decontamination technique, which was briefly explained above, the probable cluster members of the 40 OCs were identified for further analysis.

4 | ASTROPHYSICAL PARAMETERS

We have derived the fundamental parameters of 40 OCs using the decontaminated (J, $J-H$) CMDs (see Figures S1–S5) eye-fitted with Padova isochrones (Marigo et al. 2008; hereafter M08). Since the spectroscopic metal abundances $[Fe/H]_{spec}$ are available only for 21 (Col. 7, Table 4) out of 40 OCs, we have considered the abundances of $Z=+0.019$ ($[Fe/H]=0$), $Z=+0.0105$ ($[Fe/H]=-0.25$), and $Z=+0.006$ ($[Fe/H]=-0.50$), respectively. In this sense, OCs need to

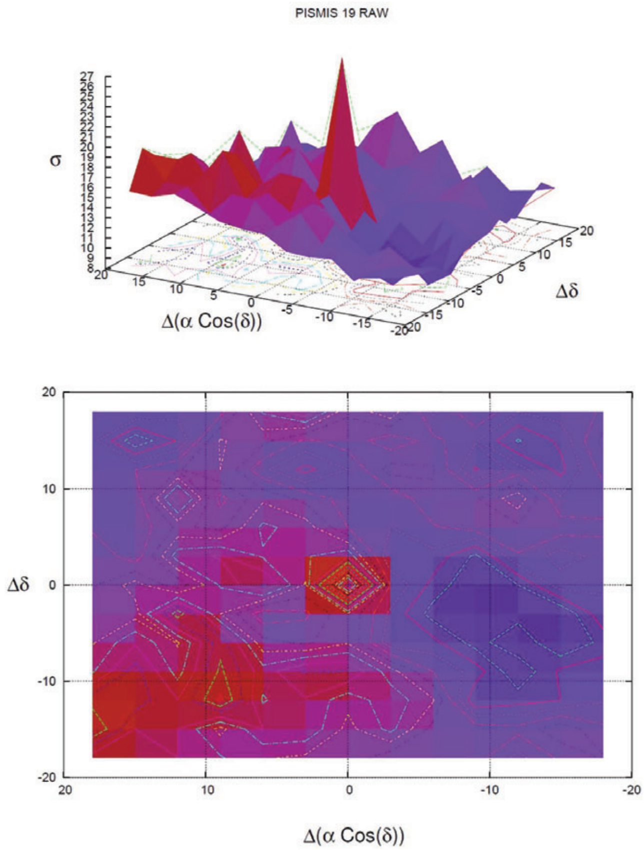

FIGURE 4 For observed (raw) photometry: (top panel) stellar surface-density σ (stars arcmin^{-2}) of Pismis 19, computed for a mesh size of $3' \times 3'$, centered on the coordinates in Table 2; (bottom panel) the corresponding isopleth surface

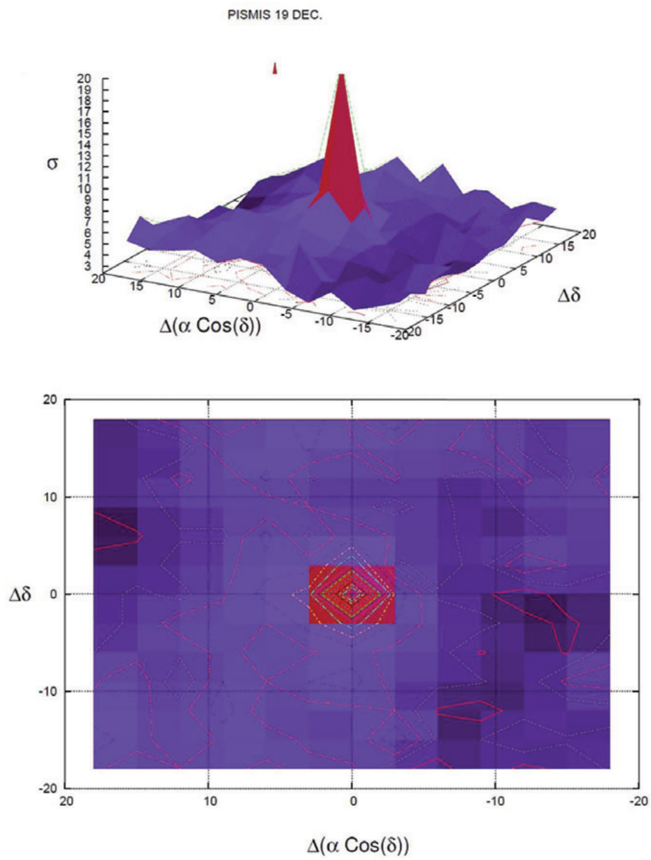

FIGURE 5 For decontaminated photometry: (top panel) stellar surface-density σ (stars arcmin^{-2}) of Pismis 19, computed for a mesh size of $3' \times 3'$, centeed on the coordinates in Table 2; (bottom panel) the corresponding isopleth surface

be uniformly and homogeneously analyzed. M08 isochrones for three Z abundances were fitted to the (J, $J-H$) CMDs of each of the 40 OCs. The most appropriate Z fit solution on the CMDs has been made by eye. Accordingly, the M08 isochrones of $Z=+0.019$ for 29 OCs, $Z=+0.0105$ for six OCs, and $Z=+0.006$ for five OCs, respectively, have provided us good fits for reddening, age, and distance modulus. As an example, such (J, $J-H$) CMDs have been displayed in Figure 6a–c for Pismis 19, for three Z abundances. The shaded areas in the panels are the color-magnitude filters, which follow the distribution of the decontaminated star sequences in the CMDs; or stars comprised in the shaded area are considered probable members. These filters are wide enough to accommodate the color distributions of main sequence and evolved stars of the clusters, allowing 1σ photometric uncertainties. The fitted 0.8 Gyr isochrone of $Z=+0.019$ for Pismis 19 in panel (a) provides a good solution. As can be seen from Figure 6a, the M08 isochrone fits well the main sequence (MS), turn-off (TO), and Red Giant/Red Clump (RG/RC) regions on the CMD of Pismis 19. Because of the presence of binaries, the M08 isochrones have been shifted to the left and below of the main sequence in Figure 6a–c, and all CMDs of the 40 OCs are presented in Figures S1–S5. The reddening, distance modulus (i.e., distance), age, and the appropriate Z abundances were derived this way for all 40 OCs of our sample. These astrophysical parameters together with their uncertainties are presented in Table 3.

However, the reddening is degenerate with the metallicity. For this, we have determined $E(B-V)$, d (pc), and age (Gyr) of 21 OCs (Table 4) for three Z abundances. The $E(B-V)$ and d (pc) values (Table 4) of three Z abundances are reasonably close to our original ones (Table 3) within uncertainties. The age values (Col. 6, Table 4) derived from three Z values are the same. As stated by Bonatto & Bica (2009a), any metallicity for the range of $+0.006 \leq Z \leq +0.019$ would produce acceptable solutions for the astrophysical parameters because of the filters of 2MASS.

Our derived ages here are almost robust enough to allow inferences about cluster evolution. For this, NGC 2286 (Figure 7) is presented as an example. The 0.8 Gyr (blue line), 1 Gyr (solid black line), and 1.2 Gyr (red line) isochrones of $Z=+0.019$ for NGC 2286 are fitted to the CMD of the cluster. As is seen from Figure 7, the 1 ± 0.2 Gyr isochrone (solid line) fits well the main sequence (MS), turn-off (TO), and Red Giant/Red Clump (RG/RC) regions on the CMD of the cluster. The uncertainties in our derived ages of 40 OCs are in the level of ±0.02–0.5 Gyr (Table 3), except for Be 36 (±1 Gyr).

JHK photometry is insensitive to metallicity, in contrast to optical photometry where the blue (B) and principally the ultraviolet (U) are sensitive to the photospheric metal lines,

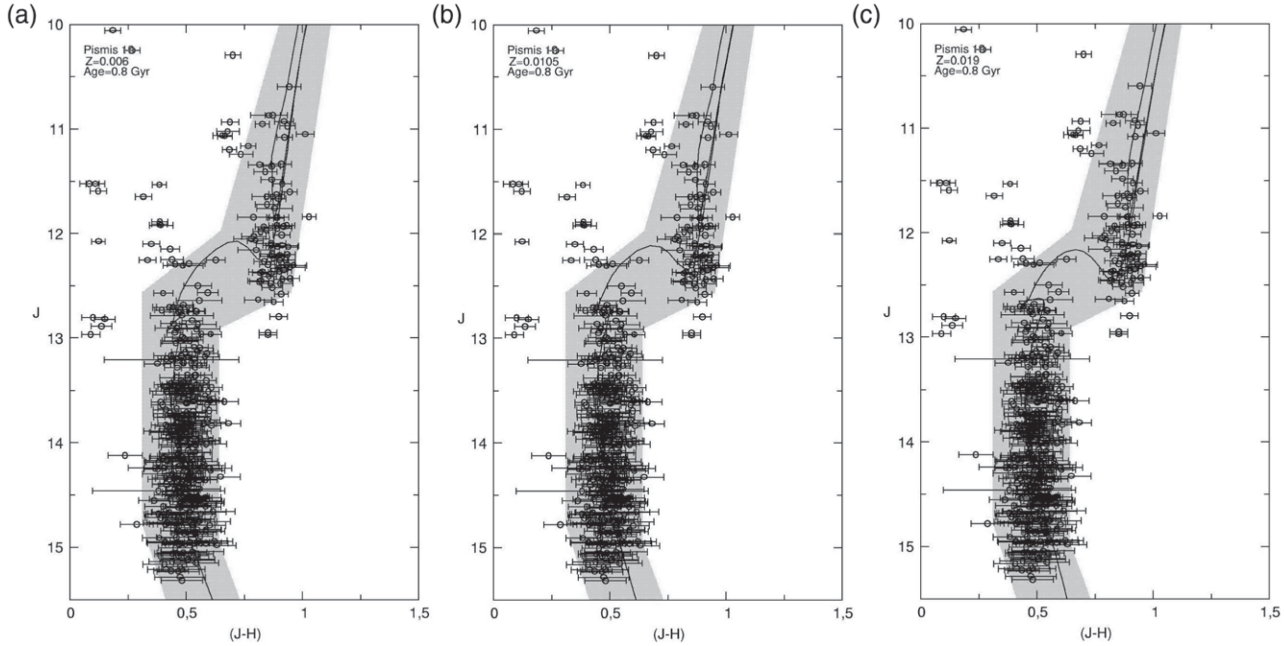

FIGURE 6 Observed decontaminated $J \times (J-H)$ CMDs extracted from the region of $R = 11'.03$ for Pismis 19. The solid lines in the panels represent the fitted 0.8 Gyr Padova isochrones for $Z = +0.019$ (solar), $Z = +0.0105$, and $Z = +0.006$, respectively. The CMD filter used to isolate cluster MS/evolved stars is shown with the shaded area

reaching its maximum blanketing effect by SpT F5. For later than SpT = G2, it becomes too fuzzy to disentangle it from the molecular lines. On the other hand, metallicity affects significantly the distance and the age of a cluster, i.e., the less the Z, the shorter the distance and the larger the age.

The reddenings $E(J-H)$ (Col. 3 in Table 3) of the 40 OCs were derived from the CMD diagrams. These are converted to $E(B-V)$ (Col. 4 in Table 3) with the extinction law $A_J/A_V = 0.276$, $A_H/A_V = 0.176$, $A_{K_s}/A_V = 0.118$, $A_J = 2.76 \times E(J-H)$, and $E(J-H) = 0.33 \times E(B-V)$ (Dutra et al. 2002), assuming a constant total-to-selective absorption ratio $R_v = 3.1$. The distance moduli of the clusters have been derived and listed in Col. 6 of Table 3. The estimated heliocentric d (kpc) and its corresponding galactocentric R_{GC} (kpc) distances are given in Cols. 7 and 8, respectively. When estimating the R_{GC} distances, we adopted the galactocentric distance of the sun as $R_{\odot} = 7.2 \pm 0.3$ kpc of Bica et al. (2006a).

The errors in $E(J-H)$, hence in color excess $E(B-V)$, distance moduli, and ages, given in Table 3 have been estimated as follows:

1. The uncertainties of $E(J-H)$ were estimated moving the M08 isochrones up and down, back and forward, and in direction of the reddening vector in the color versus magnitude diagram $(J, J-H)$ until a good fit with the observed MS, TO, the subgiant branch (SG), and RG/RC sequences was achieved.
2. The uncertainties of distance moduli in Table 3 stem to a lesser degree from the photometric errors and fitting the appropriate isochrone to the observational data points in the CMDs. A larger uncertainty, up to 2 mag in the distance moduli, originates from the assumption of the metallicity: for a larger Z the OCs are more distant, and metal-poor stars are nearer.
3. For the uncertainties in the age estimates, see those of the distance moduli. Again, metal-rich stars are younger than the metal-poor ones.

The precision of the parameters depends on the scatter of the data points in the CMDs. The uncertainties of distance moduli in Table 3 stem from fitting the appropriate isochrone to the observation in the CMDs, by taking into account the uncertainties of the photometric data. The uncertainties of distance moduli of 40 OCs are at the level of 0.10–0.31. The uncertainty of age is obtained from fitting the M08 isochrone with the appropriate heavy element to the CMDs. In this regard, the uncertainty of the age depends on the uncertainties of $E(J-H)$ and distance moduli of 40 OCs. The uncertainties of the ages of 40 OCs in Table 3 fall in the range 0.02–1.0 Gyr.

The relations of $E(B-V)$ versus galactic longitude $l°$ and $E(B-V)$ versus galactic latitude $b°$ as a function of the cluster distances, are displayed in Figure 8a,b, respectively. In the figure, the open and filled circles show the $d = [0, 2.1]$ kpc and $d = [2.1, 5.42]$ kpc subsets, respectively. The reddenings of the OCs in the anticenter directions have $0.03 \leq E(B-V) \leq 1.31$. From panel (a), the bulk of the 40 clusters lies within $|b| \leq 5°$ and $0.03 \leq E(B-V) \leq 1.31$. There are two OCs with $E(B-V) > 0.50$ in the galactic center directions.

The reddenings of 40 OCs have been compared with those of the dust maps of Schlegel et al. (1998) (hereafter SFD), which are based on the COBE/DIRBE and IRAS/ISSA maps. These maps take into account the dust absorption $E(B-V)_{\infty}$ all the way to infinity.

TABLE 3 Derived fundamental astrophysical parameters from 2MASS JHKs photometry of 40 OCs

Cluster	Z	$E(J-H)$	$E(B-V)$	Age (Gyr)	$(m-M)j$	d (kpc)	R_{GC} (kpc)
NGC 436	0.019	0.13 ± 0.03	0.42 ± 0.10	0.4 ± 0.1	12.54 ± 0.31	3.22 ± 0.46	9.48 ± 0.28
King 5	0.0105	0.26 ± 0.05	0.83 ± 0.16	1.0 ± 0.2	11.53 ± 0.24	2.03 ± 0.23	8.93 ± 0.18
NGC 1513	0.019	0.23 ± 0.02	0.74 ± 0.06	0.1 ± 0.02	10.37 ± 0.28	1.18 ± 0.15	8.29 ± 0.13
Be 15	0.019	0.27 ± 0.03	0.86 ± 0.10	0.5 ± 0.1	12.45 ± 0.31	3.10 ± 0.44	10.21 ± 0.42
NGC 1798	0.0105	0.16 ± 0.04	0.51 ± 0.13	1.5 ± 0.3	13.51 ± 0.26	5.03 ± 0.59	12.07 ± 0.55
Be 17	0.006	0.26 ± 0.04	0.83 ± 0.13	5.0 ± 0.5	11.93 ± 0.29	2.43 ± 0.33	9.65 ± 0.33
NGC 1907	0.019	0.18 ± 0.03	0.58 ± 0.10	0.4 ± 0.1	11.45 ± 0.26	1.95 ± 0.24	9.16 ± 0.23
NGC 2112	0.019	0.20 ± 0.04	0.64 ± 0.13	2.0 ± 0.3	10.15 ± 0.23	1.07 ± 0.11	8.18 ± 0.10
Koposov 12	0.0105	0.07 ± 0.02	0.22 ± 0.06	1.8 ± 0.2	11.56 ± 0.18	2.05 ± 0.17	9.26 ± 0.17
NGC 2158	0.019	0.05 ± 0.01	0.16 ± 0.03	2.5 ± 0.3	13.21 ± 0.10	4.39 ± 0.21	11.59 ± 0.21
Koposov 53	0.019	0.01 ± 0.00	0.03 ± 0.02	1.0 ± 0.1	13.05 ± 0.18	4.08 ± 0.34	11.28 ± 0.34
NGC 2194	0.019	0.13 ± 0.04	0.42 ± 0.13	0.8 ± 0.2	11.87 ± 0.27	2.37 ± 0.30	9.51 ± 0.28
NGC 2192	0.019	0.01 ± 0.00	0.03 ± 0.00	1.3 ± 0.1	13.12 ± 0.15	4.21 ± 0.29	11.37 ± 0.28
NGC 2243	0.0105	0.01 ± 0.00	0.03 ± 0.00	2.0 ± 0.2	13.37 ± 0.12	4.73 ± 0.26	10.36 ± 0.14
Trumpler 5	0.006	0.24 ± 0.05	0.77 ± 0.16	3.0 ± 0.3	12.19 ± 0.29	2.74 ± 0.36	9.80 ± 0.33
Col 110	0.019	0.06 ± 0.01	0.19 ± 0.03	3.0 ± 0.2	11.93 ± 0.15	2.44 ± 0.17	9.41 ± 0.15
NGC 2262	0.0105	0.11 ± 0.01	0.35 ± 0.03	1.3 ± 0.1	12.36 ± 0.30	2.96 ± 0.41	9.88 ± 0.35
NGC 2286	0.019	0.03 ± 0.00	0.10 ± 0.02	1.0 ± 0.2	11.82 ± 0.30	2.31 ± 0.32	9.20 ± 0.26
NGC 2309	0.019	0.16 ± 0.02	0.51 ± 0.06	0.5 ± 0.1	12.41 ± 0.21	3.03 ± 0.29	9.74 ± 0.22
Tombaugh 2	0.019	0.35 ± 0.05	1.12 ± 0.16	3.0 ± 0.3	10.43 ± 0.24	1.22 ± 0.14	8.01 ± 0.08
Be 36	0.019	0.12 ± 0.02	0.38 ± 0.06	3.0 ± 1.0	13.67 ± 0.16	5.42 ± 0.40	11.59 ± 0.27
Haffner 8	0.006	0.06 ± 0.02	0.19 ± 0.06	1.0 ± 0.1	11.98 ± 0.16	2.49 ± 0.18	9.09 ± 0.12
Mel 71	0.019	0.01 ± 0.00	0.03 ± 0.02	1.5 ± 0.2	11.54 ± 0.15	2.03 ± 0.14	8.69 ± 0.09
NGC 2425	0.019	0.10 ± 0.02	0.32 ± 0.06	3.2 ± 0.5	12.27 ± 0.26	2.85 ± 0.34	9.26 ± 0.21
NGC 2506	0.006	0.03 ± 0.01	0.10 ± 0.03	2.0 ± 0.3	12.27 ± 0.20	2.84 ± 0.26	9.27 ± 0.17
Pismis 3	0.006	0.33 ± 0.02	1.06 ± 0.06	3.2 ± 0.2	11.19 ± 0.11	1.73 ± 0.09	7.77 ± 0.03
NGC 2660	0.019	0.13 ± 0.03	0.42 ± 0.10	1.5 ± 0.3	11.89 ± 0.17	2.39 ± 0.19	7.76 ± 0.06
NGC 3680	0.019	0.05 ± 0.01	0.16 ± 0.03	1.5 ± 0.2	10.16 ± 0.10	1.08 ± 0.05	7.00 ± 0.02
Ru 96	0.019	0.07 ± 0.01	0.22 ± 0.03	1.0 ± 0.1	12.01 ± 0.25	2.52 ± 0.29	6.53 ± 0.15
Ru 105	0.019	0.05 ± 0.01	0.16 ± 0.03	1.0 ± 0.4	11.56 ± 0.20	2.05 ± 0.19	6.41 ± 0.10
Trumpler 20	0.019	0.10 ± 0.03	0.32 ± 0.10	1.5 ± 0.5	12.52 ± 0.31	3.20 ± 0.46	6.19 ± 0.27
Pismis 19	0.019	0.41 ± 0.03	1.31 ± 0.10	0.8 ± 0.1	11.42 ± 0.38	1.92 ± 0.34	6.02 ± 0.24
NGC 6134	0.019	0.10 ± 0.01	0.32 ± 0.03	1.5 ± 0.1	10.22 ± 0.12	1.11 ± 0.06	6.23 ± 0.06
IC 4651	0.019	0.02 ± 0.00	0.06 ± 0.02	2.5 ± 0.3	9.64 ± 0.20	0.85 ± 0.08	6.44 ± 0.07
NGC 6802	0.019	0.23 ± 0.03	0.74 ± 0.10	0.9 ± 0.1	11.77 ± 0.31	2.25 ± 0.32	6.22 ± 0.19
NGC 6819	0.019	0.02 ± 0.00	0.06 ± 0.02	2.5 ± 0.5	11.84 ± 0.15	2.34 ± 0.16	6.96 ± 0.06
Be 89	0.019	0.23 ± 0.02	0.74 ± 0.06	2.0 ± 0.5	12.37 ± 0.21	2.97 ± 0.28	7.47 ± 0.11
NGC 6939	0.019	0.12 ± 0.03	0.38 ± 0.10	2.0 ± 0.3	11.27 ± 0.31	1.79 ± 0.26	7.61 ± 0.06
NGC 7142	0.019	0.13 ± 0.03	0.42 ± 0.10	2.5 ± 0.3	12.04 ± 0.22	2.56 ± 0.25	8.27 ± 0.10
NGC 7789	0.0105	0.08 ± 0.02	0.26 ± 0.06	1.8 ± 0.2	11.23 ± 0.21	1.76 ± 0.17	8.13 ± 0.08

The relations of $E(B-V)_{\mathrm{SFD},\infty}$ versus $E(B-V)$, and $E(B-V)_{\mathrm{SFD}}$ versus $E(B-V)$ of the 40 OCs are displayed in Figure 9a,b, respectively. As is seen from Figure 9a, the values of $E(B-V)_{\mathrm{SFD},\infty}$ are at the level of $0.07 \leq E(B-V)_{\mathrm{SFD},\infty} \leq 25.81$. For seven clusters, differences in between both reddenings are $\Delta E(B-V) \leq 0.10$, while the differences of 33 OCs are larger than 0.10 mag. The equation given by Bonifacio et al. (2000) has been adopted to correct the SFD reddening estimates. Then the final reddening, $E(B-V)_{\mathrm{SFD}}$, for a given star is reduced compared to the total reddening $E(B-V)$ (l, $b)_\infty$ by a factor $\{1-\exp[-d\sin|b|/H]\}$, given by Bahcall & Soneira (1980), where b, d, and H are the galactic latitude (Col. 9 of Table 2), the distance from the observer to the object (Col. 7 of Table 3), and the scale height of the dust layer in the galaxy, respectively. The value of $H = 125$ pc is adopted (Bonifacio et al. 2000). The reduced final reddenings have been compared with the ones of 40 OCs in Figure 9b. The reduced $E(B-V)$ values fall in the range $0.07 \leq E(B-V) \leq 1.261$.

There are significant differences for 27 OCs between both $E(B-V)$ color excess values. For the rest, the $E(B-V)$ values of 13 OCs are quite close to the ones of SFD. Note that

TABLE 4 Z, $E(B-V)$, d (pc), and age (Gyr) of 21 OCs with $[Fe/H]_{spec}$. $E(B-V)$ values are listed in Col. 3 for three Z abundances of 21 OCs in our sample. $[Fe/H]_{iso}$ values in Col. 4 are converted from the expression $Z = Z_{\odot} \cdot 10^{[Fe/H]}$. The solar abundance value is taken as $Z_{\odot} = +0.019$. Ages are given in Col. 6. $[Fe/H]_{spec}$ values together with literature are listed in Col. 7 and 8

Cluster	Z	$E(B-V)$	$[Fe/H]_{iso}$	d (kpc)	Age (Gyr)	$[Fe/H]_{spec}$	Reference
Trumpler 5	0.019	0.54 ± 0.13		3.13 ± 0.39	3		
	0.0105	0.70 ± 0.16		2.87 ± 0.38	3		
	0.006	0.77 ± 0.16	−0.50	2.74 ± 0.36	3	−0.36	Carrera et al. (2007)
NGC 2158	0.019	0.16 ± 0.03	0	4.39 ± 0.21	2.5	−0.28	Jacobson et al. (2011)
	0.0105	0.29 ± 0.03		3.98 ± 0.19	2.5		
	0.006	0.38 ± 0.03		3.75 ± 0.18	2.5		
Col 110	0.019	0.19 ± 0.03	0	2.44 ± 0.17	3	−0.01	Carrera et al. (2007)
	0.0105	0.29 ± 0.06		2.29 ± 0.17	3		
	0.006	0.42 ± 0.06		2.03 ± 0.15	3		
NGC6134	0.019	0.32 ± 0.03	0	1.11 ± 0.06	1.5	0.12	Smiljanic et al. (2009)
	0.0105	0.48 ± 0.06		0.97 ± 0.07	1.5		
	0.006	0.64 ± 0.10		0.85 ± 0.07	1.5		
NGC2425	0.019	0.32 ± 0.06	0	2.85 ± 0.34	3.2	−0.15	Jacobson et al. (2011)
	0.0105	0.42 ± 0.10		2.74 ± 0.33	3.2		
	0.006	0.51 ± 0.16		2.64 ± 0.35	3.2		
Trumpler 20	0.019	0.32 ± 0.10	0	3.20 ± 0.46	1.5	0.09	Carraro et al. (2014)
	0.0105	0.48 ± 0.10		2.80 ± 0.40	1.5		
	0.006	0.64 ± 0.10		2.45 ± 0.35	1.5		
NGC 2112	0.019	0.64 ± 0.13	0	1.07 ± 0.11	2	−0.10	Brown et al. (1996)
	0.0105	0.77 ± 0.06		0.87 ± 0.12	2		
	0.006	0.90 ± 0.06		0.77 ± 0.09	2		
Mel 71	0.019	0.03 ± 0.02	0	2.03 ± 0.14	1.5	−0.30	Brown et al. (1996)
	0.0105	0.16 ± 0.06		1.93 ± 0.14	1.5		
	0.006	0.29 ± 0.06		1.92 ± 0.17	1.5		
NGC 7789	0.019	0.19 ± 0.03		1.81 ± 0.17	1.8		
	0.0105	0.26 ± 0.06	−0.25	1.76 ± 0.17	1.8	0.02	Jacobson et al. (2011)
	0.006	0.32 ± 0.06		1.72 ± 0.19	1.8		
NGC 3680	0.019	0.16 ± 0.03	0	1.08 ± 0.05	1.5	0.04	Smiljanic et al. (2008)
	0.0105	0.32 ± 0.06		0.95 ± 0.06	1.5		
	0.006	0.48 ± 0.10		0.85 ± 0.07	1.5		
IC 4651	0.019	0.06 ± 0.02	0	0.85 ± 0.08	2.5	0.10	Pasquini et al. (2004)
	0.0105	0.16 ± 0.03		0.78 ± 0.08	2.5		
	0.006	0.26 ± 0.06		0.72 ± 0.08	2.5		
NGC 6819	0.019	0.06 ± 0.02	0	2.34 ± 0.16	2.5	0.09	Bragaglia et al. (2001)
	0.0105	0.16 ± 0.03		2.15 ± 0.18	2.5		
	0.006	0.32 ± 0.10		1.84 ± 0.15	2.5		
NGC 1798	0.019	0.32 ± 0.06		5.69 ± 0.54	1.5		
	0.0105	0.51 ± 0.13	−0.25	5.03 ± 0.59	1.5	−0.12	Carrera (2012)
	0.006	0.7 ± 0.16		4.45 ± 0.58	1.5		
NGC 2243	0.019	0.005 ± 0.005		5.01 ± 0.23	2		
	0.0105	0.03 ± 0.005	−0.25	4.73 ± 0.26	2	−0.48	Gratton & Contarini (1994)
	0.006	0.16 ± 0.03		4.49 ± 0.25	2		
NGC 6939	0.019	0.38 ± 0.10	0	1.79 ± 0.26	2	0	Jacobson et al. (2007)
	0.0105	0.45 ± 0.13		1.64 ± 0.26	2		
	0.006	0.58 ± 0.19		1.50 ± 0.26	2		
NGC 7142	0.019	0.42 ± 0.10	0	2.56 ± 0.25	2.5	0.08	Jacobson et al. (2008)
	0.0105	0.54 ± 0.13		2.32 ± 0.26	2.5		
	0.006	0.67 ± 0.16		2.11 ± 0.25	2.5		
NGC 2194	0.019	0.42 ± 0.13	0	2.37 ± 0.30	0.8	−0.08	Jacobson et al. (2011)
	0.0105	0.51 ± 0.16		2.15 ± 0.26	0.8		
	0.006	0.61 ± 0.16		1.97 ± 0.24	0.8		
NGC 2660	0.019	0.42 ± 0.10	0	2.39 ± 0.19	1.5	0.04	Bragaglia et al. (2008)

TABLE 4 Continued

Cluster	Z	E(B − V)	[Fe/H]$_{iso}$	d (kpc)	Age (Gyr)	[Fe/H]$_{spec}$	Reference
	0.0105	0.51 ± 0.13		2.20 ± 0.19	1.5		
	0.006	0.67 ± 0.16		1.97 ± 0.21	1.5		
Be 17	0.019	0.64 ± 0.13		3.02 ± 0.38	5		
	0.0105	0.74 ± 0.13		2.71 ± 0.40	5		
	0.006	0.83 ± 0.13	−0.50	2.43 ± 0.33	5	−0.10	Friel et al. (2005)
Tombaugh 2	0.019	1.12 ± 0.16	0	1.22 ± 0.14	3	−0.45	Brown et al. (1996)
	0.0105	1.22 ± 0.19		1.18 ± 0.14	3		
	0.006	1.31 ± 0.19		1.13 ± 0.18	3		
NGC 2506	0.019	0.02 ± 0.005		3.07 ± 0.28	2		
	0.0105	0.06 ± 0.03		2.94 ± 0.27	2		
	0.006	0.10 ± 0.03	−0.50	2.84 ± 0.26	2	−0.20	Carretta et al. (2004)

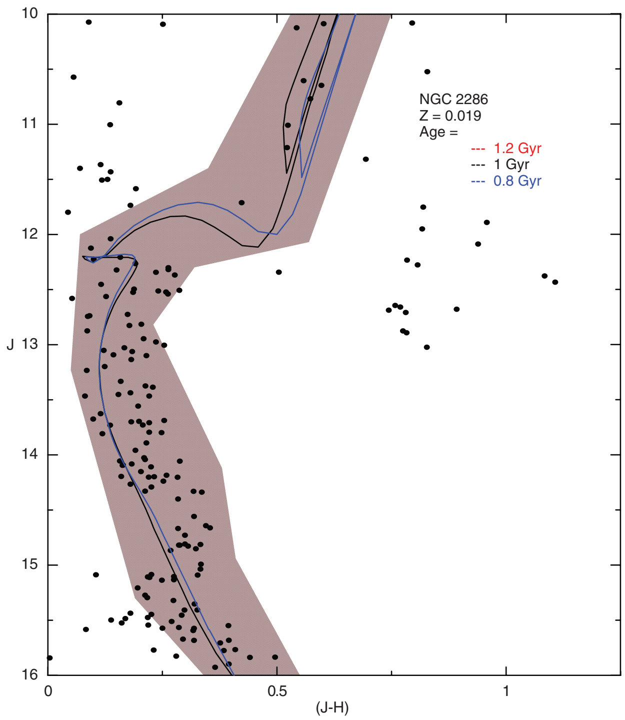

FIGURE 7 Observed decontaminated $J \times (J - H)$ CMD of NGC 2286. The solid lines in the panels represent the fitted 0.8 Gyr (blue line), 1 Gyr (solid black line), and 1.2 Gyr (red line) isochrones of $Z = +0.019$. The CMD filter used to isolate cluster MS/evolved stars is shown with the shaded area

SFD maps are not reliable at regions $|b| < 5°$ due to contaminating sources and uncertainties in the dust temperatures (Gonzalez et al. 2012). Therefore, the SFD values resulted from line-of-sight integral through the Milky Way and with low spatial resolution, and it is quite normal to have different reddening values for these relatively close (∼1 kpc) star clusters.

5 | STRUCTURAL PARAMETERS

We derived the structural parameters of 40 OCs from the stellar RDPs. Usually, the RDPs of star clusters can be described by an analytical profile, like the empirical,

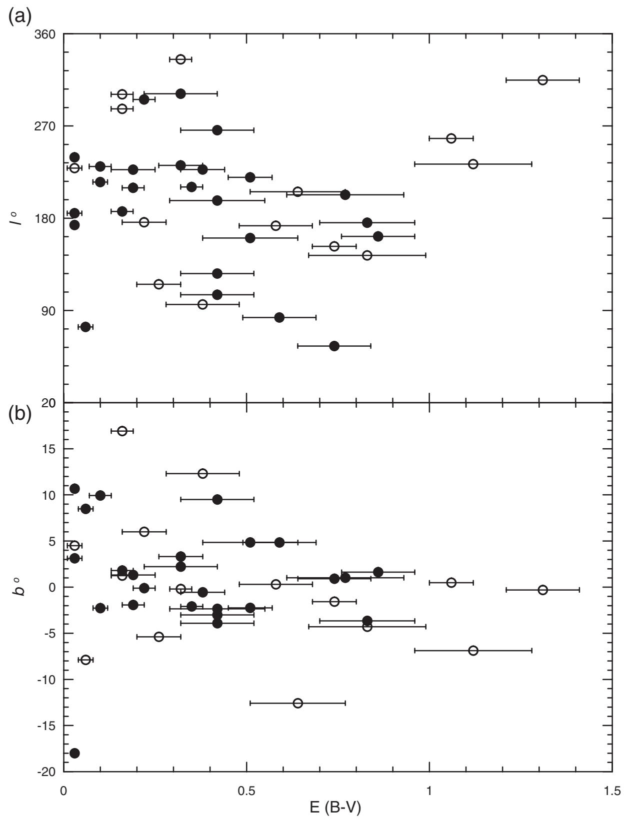

FIGURE 8 $E(B - V)$ versus $l°$ (panel a) and versus $b°$ (panel b) for the 40 OCs. Open and filled circles show clusters with $d = [0, 2.1]$ kpc and $d = [2.1, 5.42]$ kpc, respectively

single-mass, modified isothermal spheres of King (1966) and Wilson (1975), and the power law with a core of Elson et al. (1987). These functions are characterized by different sets of parameters that are related to the cluster structure. Here we adopted the two-parameter function $\sigma(R) = \sigma_{bg} + \sigma_0/(1 + (R/R_c)^2)$, where σ_{bg} is the residual background density, σ_0 the central density of stars, and R_{core} the core radius. Applied to star counts, this function is similar to that used by King (1962) to describe the surface brightness profiles in the central parts of globular clusters. To minimize the degrees of freedom in RDP fits with the King-like profile, σ_{bg} was kept fixed (measured in the respective comparison

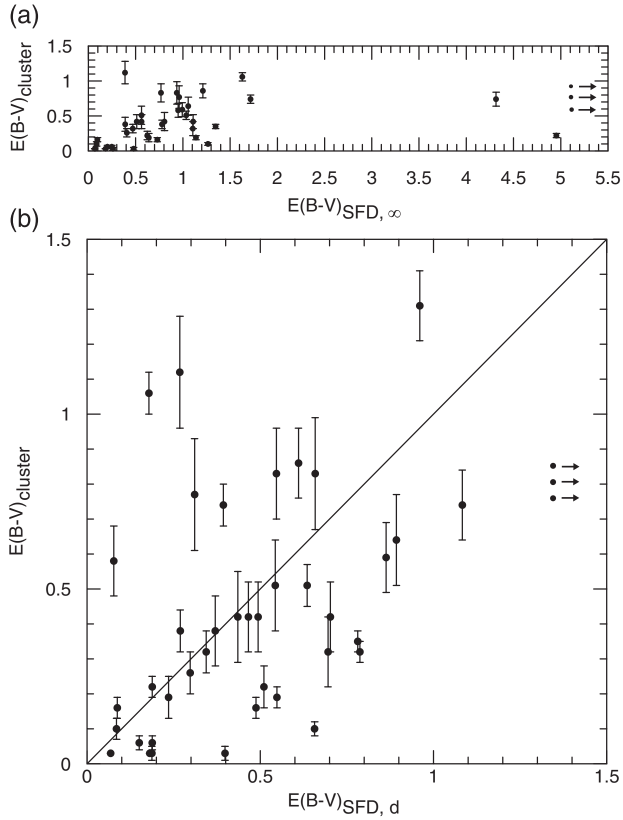

FIGURE 9 Relations of $E(B-V)$cluster $- E(B-V)_{\mathrm{SFD},\infty}$ (panel a), $E(B-V)$cluster $- E(B-V)_{\mathrm{SFD,d}}$ (panel b), respectively

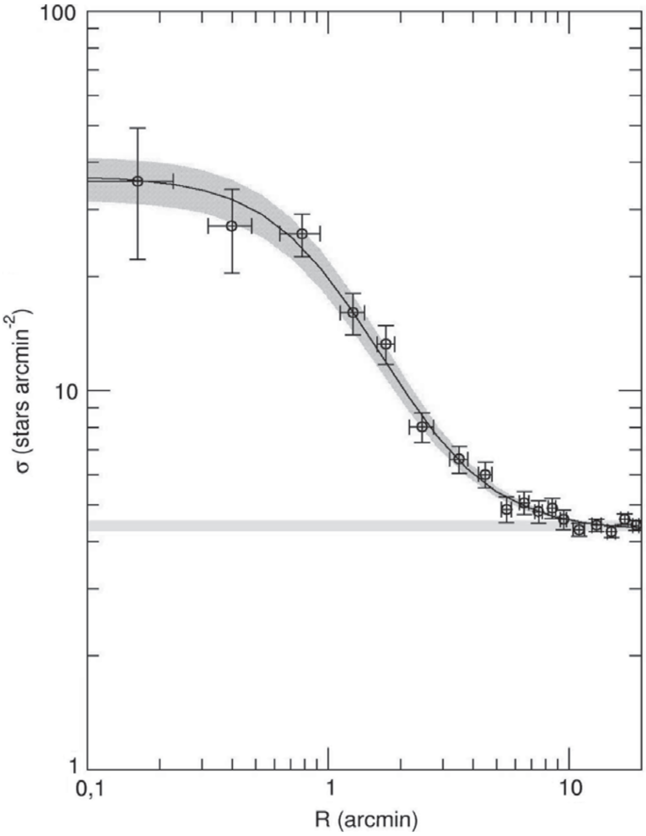

FIGURE 10 Stellar RDP (open circles) of Pismis 19 built with CMD filtered photometry. Solid line shows the best fit King profile. Horizontal red bar: stellar background level measured in the comparison field. Shaded region: 1σ King fit uncertainty

fields) while σ_0 and R_{core} were determined by the best profile fit to the data. As a representative of the OCs sample, the RDP of Pismis 19 fitted with King's profile is shown in Figure 10, where the solid line shows the best profile fit. The horizontal red bar in the figure denotes the stellar background level measured in the comparison field, and the 1σ profile fit uncertainty is shown by the shaded domain. The stellar RDP fitted profiles of the 40 OCs are given in Figures S6–S9. The cluster radius (R_{RDP}) is also obtained from the measured distance from the cluster center where the RDP and residual background are statistically indistinguishable (Bonatto & Bica 2007a). R_{RDP} can be taken as an observational truncation radius whose value depends on the radial distribution of member stars and the stellar field density. ΔR means the wide external ring of the stellar comparison field (see also Section 3). These structural parameters and their meaning are given in Table 5.

From the distributions of R_{core} and R_{RDP}, given in Figure 11a,b, there seems to be two groupings at $R_{\mathrm{RDP}} = 7$ pc and $R_{\mathrm{core}} = 1.5$ pc, respectively, which are close to the values of 10 pc and 1.5 pc of Bukowiecki et al. (2011).

6 | MASS AND MASS FUNCTIONS

The stellar masses stored in the OCs of our sample have been determined by means of their MFs, built for the observed MS mass range, according to Bica et al. (2006b). By following the algorithm, which is basically defined by Bonatto & Bica (2005), luminosity functions from the decontaminated (J, $J-H$) diagrams of the OCs have been transformed into MFs through the corresponding mass versus luminosity relations derived from the M08 isochrones, which correspond to the ages in Col. 5 of Table 3. We determined the overall masses of 26 OCs and the core masses of 24 OCs in our sample. The total mass locked up in stars of these OCs was obtained by considering all stars from the turn-off to the H-burning mass limit. We do this by directly extrapolating the low-mass MFs down to $0.08\,M_{\odot}$. Here, we have based our results on the CMD filtered photometry of open cluster and offset field stars. The filtering process contemplates most of the background, leaving a residual contamination. Because of the relatively large sizes of the OCs and the brightness limitation of the 2MASS photometry, we do not have access to the whole stellar mass range of the OCs. Here, we stress that the values we derived should be taken as approximations.

The relation of $\varphi(m)$ (stars $m_{\odot}^{-1}$) versus $m_{\odot}$ of our representative open cluster Pismis 19 is shown in Figure 12a,c for different cluster regions. The main sequence MFs in the panels (a)–(c) of Figure 12 are fitted with the function $\varphi(m) \propto m^{-(1+\chi)}$, and the MF slopes ($\chi$) have been determined for the different segments of the mass function MF in Col. 1 of Table 6. More details of this approach are given in Table 6,

TABLE 5 Structural parameters of 40 OCs. Column 2 represents arcmin to parsec scale. σ_{0K} in Cols. 3 and 7 is the central density of stars. σ_{bg} in Cols. 4 and 8 is the residual background density. R_{core} in Cols. 5 and 8 and R_{RDP} in Cols. 6 and 10 are the core and cluster radii, respectively. The symbols $*\,pc^{-2}$ and $*'^{-2}$ in Cols. 3, 4, 7, and 8 mean stars pc^{-2} and stars $arcmin^{-2}$, respectively. $\Delta R(')$ in Col. 11 denotes comparison field ring. Column 12 represents the correlation coefficient

Cluster	(1′) pc	σ_{0K} (*, pc^{-2})	σ_{bg} (*, pc^{-2})	R (pc)	R_{RDP} (pc)	σ_{0K} ($*'^{-2}$)	σ_{bg} ($*'^{-2}$)	R_{core} (′)	R_{RDP} (′)	$\Delta R(')$	CC
NGC 436	0.94	10.94 ± 2.97	0.71 ± 0.03	1.04 ± 0.20	6.97 ± 0.26	9.60 ± 2.60	0.62 ± 0.03	1.11 ± 0.22	7.44 ± 0.27	22–32	0.93
King 5	0.59	24.79 ± 5.28	2.70 ± 0.06	0.95 ± 0.15	5.62 ± 0.18	8.65 ± 1.84	0.94 ± 0.02	1.60 ± 0.25	9.52 ± 0.30	20–30	0.94
NGC 1513	0.34	30.60 ± 4.73	17.44 ± 0.44	1.65 ± 0.26	6.51 ± 0.20	3.61 ± 0.55	2.05 ± 0.05	4.80 ± 0.75	16.99 ± 0.58	42–57	0.94
Be 15	0.90	25.70 ± 11.33	0.97 ± 0.02	0.35 ± 0.10	5.04 ± 0.30	20.89 ± 9.20	0.79 ± 0.02	0.39 ± 0.11	5.59 ± 0.33	30–40	0.86
NGC 1798	1.46	6.64 ± 1.90	0.58 ± 0.01	1.10 ± 0.22	9.11 ± 0.48	18.20 ± 5.22	1.59 ± 0.03	0.67 ± 0.13	5.51 ± 0.29	50–60	0.92
Be 17	0.71	7.25 ± 1.38	3.26 ± 0.10	2.10 ± 0.39	5.29 ± 0.20	3.62 ± 0.69	1.63 ± 0.05	2.98 ± 0.55	7.48 ± 0.29	42–52	0.94
NGC 1907	0.57	17.03 ± 4.16	4.32 ± 0.19	1.28 ± 0.27	4.26 ± 0.16	5.47 ± 1.34	1.39 ± 0.06	2.26 ± 0.47	7.50 ± 0.28	50–60	0.91
NGC 2112	0.31	24.69 ± 3.51	6.96 ± 0.21	1.64 ± 0.21	5.92 ± 0.19	2.39 ± 0.34	0.67 ± 0.02	5.28 ± 0.68	19.01 ± 0.61	50–60	0.95
Koposov 12	0.60	8.96 ± 3.74	1.27 ± 0.05	0.87 ± 0.27	3.82 ± 0.20	3.18 ± 1.33	0.45 ± 0.02	1.46 ± 0.46	6.41 ± 0.33	15–25	0.83
NGC 2158	1.27	28.85 ± 4.67	1.45 ± 0.06	1.74 ± 0.20	14.03 ± 0.71	47.05 ± 7.61	2.37 ± 0.10	1.36 ± 0.16	10.99 ± 0.56	45–60	0.97
Koposov 53	1.18	7.12 ± 0.23	0.48 ± 0.05	0.66 ± 0.04	4.18 ± 0.33	10.04 ± 0.33	0.67 ± 0.08	0.56 ± 0.03	3.52 ± 0.28	25–35	0.99
NGC 2194	0.69	21.00 ± 3.31	3.30 ± 0.15	1.66 ± 0.22	6.55 ± 0.21	9.98 ± 1.58	1.57 ± 0.07	2.41 ± 0.32	9.5 ± 0.31	40–50	0.96
NGC 2192	1.22	5.26 ± 1.59	0.41 ± 0.01	1.11 ± 0.24	5.47 ± 0.34	7.87 ± 2.42	0.62 ± 0.02	0.91 ± 0.19	4.47 ± 0.28	45–55	0.90
NGC 2243	1.38	13.35 ± 4.18	0.22 ± 0.01	0.89 ± 0.18	12.94 ± 0.37	25.28 ± 7.95	0.42 ± 0.02	0.65 ± 0.13	9.40 ± 0.27	20–30	0.93
Trumpler 5	0.79	13.62 ± 1.72	3.37 ± 0.09	3.86 ± 0.43	15.18 ± 0.47	8.65 ± 1.09	2.14 ± 0.06	4.85 ± 0.54	19.05 ± 0.58	27–37	0.97
Col 110	0.71	5.32 ± 0.51	2.68 ± 0.05	6.25 ± 0.63	12.12 ± 0.40	2.68 ± 0.26	1.35 ± 0.02	8.79 ± 0.88	17.07 ± 0.57	40–50	0.97
NGC 2262	0.86	22.03 ± 5.17	1.93 ± 0.05	0.85 ± 0.14	6.37 ± 0.24	16.32 ± 3.81	1.43 ± 0.04	0.99 ± 0.17	7.40 ± 0.28	30–45	0.94
NGC 2286	0.67	6.81 ± 2.29	2.66 ± 0.12	1.59 ± 0.48	6.39 ± 0.19	3.07 ± 1.03	1.20 ± 0.05	2.37 ± 0.72	9.51 ± 0.29	27–37	0.85
NGC 2309	0.88	12.41 ± 5.96	0.64 ± 0.05	0.84 ± 0.28	7.50 ± 0.25	9.64 ± 4.63	0.50 ± 0.04	0.95 ± 0.32	8.51 ± 0.29	50–60	0.84
Tombaugh 2	0.35	134.29 ± 83.62	3.67 ± 0.25	0.17 ± 0.07	1.92 ± 0.11	16.91 ± 10.5	0.46 ± 0.03	0.47 ± 0.18	5.42 ± 0.31	20–25	0.98
Be 36	1.57	3.30 ± 1.76	0.51 ± 0.02	1.32 ± 0.51	10.23 ± 0.40	8.21 ± 4.39	1.27 ± 0.04	0.83 ± 0.32	6.50 ± 0.25	25–40	0.79
Haffner 8	0.72	5.31 ± 2.85	3.89 ± 0.08	1.47 ± 0.68	6.93 ± 0.21	2.79 ± 1.50	2.04 ± 0.04	2.03 ± 0.94	9.56 ± 0.29	45–60	0.69
Mel 71	0.59	22.61 ± 3.97	4.39 ± 0.09	1.27 ± 0.18	5.00 ± 0.17	7.89 ± 1.39	1.53 ± 0.03	2.16 ± 0.30	8.46 ± 0.29	45–60	0.95
NGC 2425	0.83	11.00 ± 2.04	2.28 ± 0.04	1.16 ± 0.17	5.43 ± 0.22	7.55 ± 1.41	1.57 ± 0.03	1.40 ± 0.20	6.54 ± 0.26	42–47	0.95
NGC 2506	0.82	18.56 ± 3.13	1.07 ± 0.04	1.65 ± 0.20	10.76 ± 0.48	12.67 ± 2.14	0.73 ± 0.03	2.00 ± 0.24	13.02 ± 0.58	40–50	0.96
Pismis 3	0.50	26.09 ± 2.91	6.53 ± 0.11	2.10 ± 0.20	8.58 ± 0.29	6.61 ± 0.74	1.65 ± 0.03	4.17 ± 0.40	17.05 ± 0.57	37–47	0.98
NGC 2660	0.69	90.44 ± 24.32	3.84 ± 0.09	0.39 ± 0.07	5.27 ± 0.17	43.71 ± 11.74	1.86 ± 0.04	0.55 ± 0.10	7.58 ± 0.25	25–35	0.94
NGC 3680	0.31	19.37 ± 7.61	1.84 ± 0.05	0.47 ± 0.13	2.98 ± 0.10	1.90 ± 0.75	0.18 ± 0.005	1.49 ± 0.41	9.49 ± 0.32	40–50	0.85
Ru 96	0.73	6.52 ± 2.75	5.95 ± 0.13	1.43 ± 0.53	2.60 ± 0.21	3.54 ± 1.45	3.20 ± 0.07	1.94 ± 0.73	3.54 ± 0.29	50–60	0.77
Ru 105	0.56	2.63 ± 1.81	1.52 ± 0.05	1.35 ± 0.78	3.83 ± 0.21	0.93 ± 0.64	0.54 ± 0.02	2.27 ± 1.30	6.42 ± 0.34	47–57	0.64
Trumpler 20	0.93	10.22 ± 1.22	4.73 ± 0.12	3.12 ± 0.38	13.98 ± 0.55	8.86 ± 1.06	4.10 ± 0.10	3.36 ± 0.41	15.02 ± 0.59	40–50	0.97
Pismis 19	0.56	104.06 ± 15.47	13.68 ± 0.18	0.54 ± 0.06	6.16 ± 0.33	32.46 ± 4.82	4.27 ± 0.05	0.96 ± 0.10	11.03 ± 0.59	47–57	0.97
NGC 6134	0.32	72.12 ± 24.74	7.82 ± 0.18	0.45 ± 0.11	3.08 ± 0.10	7.52 ± 2.59	0.81 ± 0.02	1.39 ± 0.34	9.53 ± 0.30	13–22	0.86
IC 4651	0.25	38.57 ± 7.88	12.50 ± 0.99	1.02 ± 0.22	2.35 ± 0.08	2.36 ± 0.48	0.76 ± 0.06	4.13 ± 0.91	9.49 ± 0.31	50–60	0.92
NGC 6802	0.65	34.48 ± 9.18	7.90 ± 0.27	1.03 ± 0.18	4.24 ± 0.18	14.72 ± 3.63	3.38 ± 0.12	1.58 ± 0.28	6.49 ± 0.38	45–60	0.92
NGC 6819	0.68	38.22 ± 4.18	3.97 ± 0.08	1.50 ± 0.12	12.92 ± 0.40	17.15 ± 1.95	1.84 ± 0.04	2.20 ± 0.18	18.98 ± 0.59	40–50	0.98
Be 89	0.88	7.02 ± 1.35	3.80 ± 0.12	2.75 ± 0.53	7.48 ± 0.26	5.42 ± 1.04	2.90 ± 0.09	3.10 ± 0.60	8.50 ± 0.30	15–20	0.93
NGC 6939	0.52	33.06 ± 5.19	3.35 ± 0.17	1.16 ± 0.15	4.92 ± 0.18	8.96 ± 1.41	0.91 ± 0.05	2.24 ± 0.28	9.46 ± 0.28	35–45	0.97
NGC 7142	0.74	10.15 ± 1.87	1.72 ± 0.10	1.98 ± 0.32	11.19 ± 0.44	5.63 ± 1.04	0.95 ± 0.05	2.65 ± 0.43	15.02 ± 0.59	50–60	0.94
NGC 7789	0.51	31.23 ± 2.22	3.88 ± 0.04	2.32 ± 0.13	26.88 ± 0.74	8.18 ± 0.58	1.02 ± 0.01	4.52 ± 0.25	52.5 ± 1.44	55–70	0.99

where we also show the number and mass of the evolved stars (m_{evol}). The MF slopes of the core (29 OCs) and the overall (31 OCs) regions of OCs are presented in Cols. 2 and 5 of Table 7. Since the lower MS is not accessible on the (J, $J - H$) diagrams of the OCs sample, we assumed that the low-mass content is still present, and use Kroupa's MF[6] to estimate the total stellar mass, down to the H-burning mass limit. The results (the number of stars, MS and evolved star contents (m_{obs}), MF slope (χ), and mass extrapolated (m_{tot}) to $0.08\,M_\odot$) for each cluster region are given in Table 6. The mass densities of ρ in unit of $M_\odot\,pc^{-3}$ are also estimated and given in Cols. 8 and 11 of Table 6 (see also Section 7.7).

When deriving the mass functions, the part of the steep that is observed in the core may come from crowding and

[6] $\chi = 0.3 \pm 0.5$ Kroupa (2001) for $0.08 < M_\odot < 0.5$, $\chi = 1.3 \pm 0.3$ for $0.5 < M_\odot < 1.0$, and $\chi = 1.3 \pm 0.7$ for $1.0 < M_\odot$.

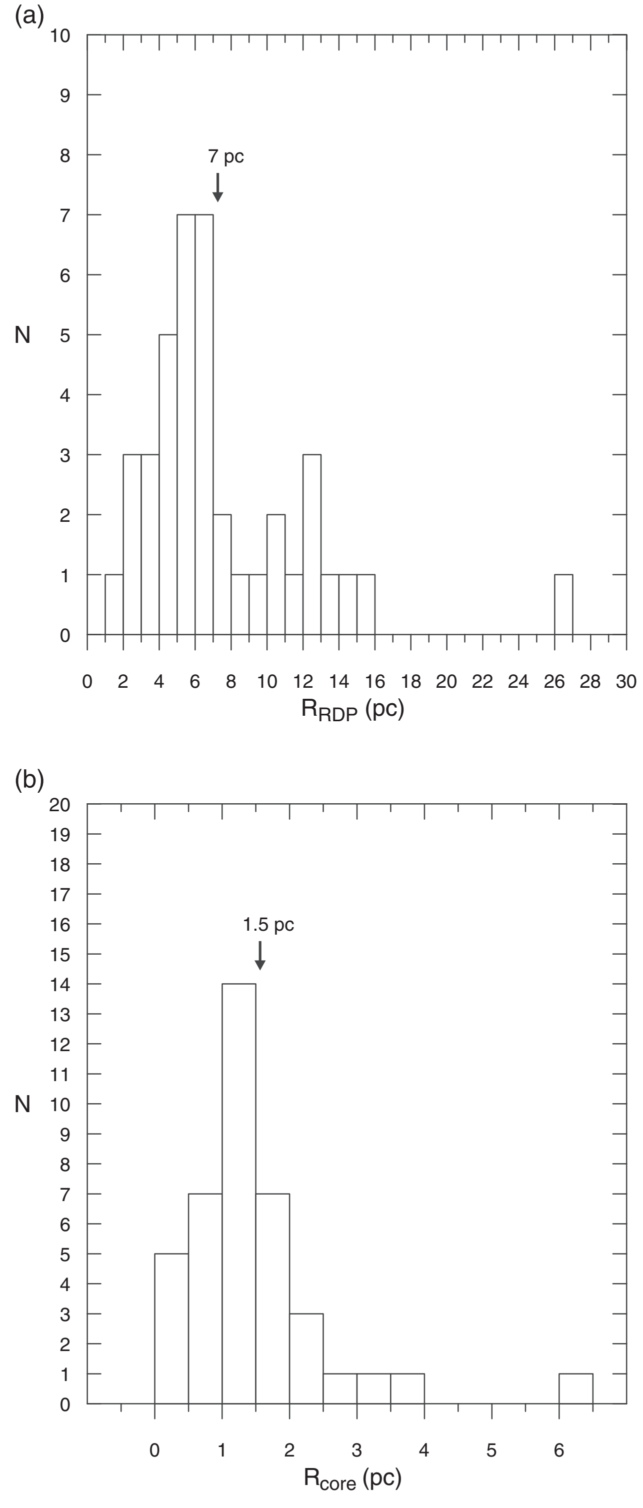

FIGURE 11 Distributions of R_{RDP} (panel a) and R_{core} (panel b) of 40 OCs, respectively

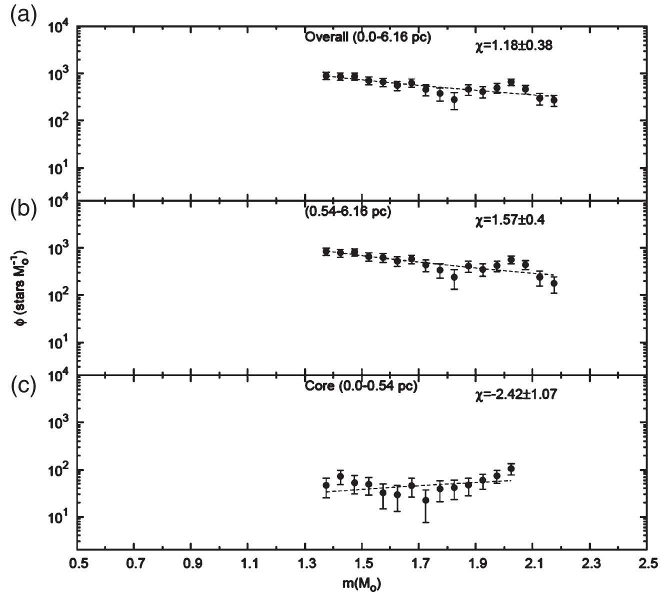

FIGURE 12 $\varphi(m)$(stars $m_\odot^{-1}$) versus $m_\odot$ of Pismis 19 cluster, as a function of distance from the core

completeness. 2MASS is not very photometrically deep and has just a moderate spatial resolution. So, in crowded regions (such as the core of most clusters), many stars are not detected, especially the faint ones. This, in turn may mimic mass segregation.

The relaxation time t_{rlx} (Myr) is the characteristic timescale for a cluster to reach some level of energy equipartition (Binney & Merrifield 1998). As discussed in Bonatto & Bica (2005, 2006, 2007a), the evolutionary parameter ($\tau = \text{age}/t_{rlx}$) appears to be a good indicator of dynamical state. Following Bonatto & Bica (2006), we parameterize t_{rlx} as $t_{rlx} \approx 0.04(N/(\ln N))(R/(1\ \text{pc}))$, where N is the number of stars located inside the region of radius R. The relaxation time and evolutionary parameter for both core and the overall regions are listed in Table 7. The uncertainties in the evolutionary parameters (τ) of OCs have been estimated by propagating the errors in age (Table 3), radii (Table 5), and N (Table 6) into t_{rlx} and τ. When propagated, the latter two errors produce a large uncertainty in t_{rlx} (Table 7) and, consequently, a large uncertainty in the evolutionary parameter. In this sense, both t_{rlx} and τ should be taken simply as an order-of-magnitude estimate.

From the overall mass distribution ($m_{overall}$) of 26 OCs displayed in Figure 13, 2,000 $M_\odot$ value is considered as a criterion in classifying the clusters as less massive and massive.

7 | RESULTS

7.1 | Relation of R_{RDP} versus R_{core}

The cluster and core radii (R_{RDP}, R_{core}) of 40 OCs, given in Figure 14 are related by the following relation: $R_{RDP} = (4.69\pm0.35)R_{core}^{(0.56\pm0.11)}$ with a mild correlation coefficient (CC, hereafter) of 0.61. This relation of Figure 14 is almost linear between log (R_{RDP}) and log (R_{core}), where the axes are in a log–log scale. Their core and cluster sizes are $0.17 \leq R_{core}$ (pc) ≤ 6.25 and $1.92 \leq R_{RDP}$ (pc) ≤ 26.88, respectively. The OCs in our sample that do not follow the relation above are either intrinsically small or have been suffering from significant evaporation effects. Our coefficient value (4.69) of Figure 14 falls in the range 3.1–8.9 of the literature (Table 8). However, the coefficients in Table 8 are affected by the

TABLE 6 Number of stars, mass information, mass function slope, and mass density, which correspond to cluster regions of available clusters for the cases of evolved, observed + evolved, and extrapolated + evolved. The full version is available in Table S6

	NGC 436									
	Evolved		χ		Observed + evolved			Extrapolated + evolved		
Region (pc)	N^* (stars)	m_{evol} ($10^1\ M_\odot$)	1.38–2.78	—	N^* (10^2 stars)	m_{obs} ($10^2\ M_\odot$)	ρ ($M_\odot$ pc^{-3})	N^* (10^2 stars)	m_{tot} ($10^2\ M_\odot$)	ρ ($M_\odot$ pc^{-3})
0.0–1.04	1 ± 1	0.4 ± 0.4	−1.46 ± 0.47	—	0.25 ± 0.03	0.56 ± 0.28	11.9 ± 5.97	0.4 ± 0.1	0.7 ± 0.03	15.2 ± 6.11
0.04–6.97	12 ± 6	3.5 ± 1.8	1.74 ± 0.36	—	1.01 ± 0.1	2 ± 0.57	0.14 ± 0.04	25.6 ± 19.6	9.8 ± 3.8	0.69 ± 0.27
0.0–6.97	14 ± 6	3.9 ± 1.9	0.86 ± 0.29	—	1.12 ± 0.09	2.55 ± 0.63	0.18 ± 0.04	17.1 ± 11.9	7.9 ± 2.4	0.56 ± 0.17
…	…	…	…	…	…	…	…	…	…	…

Col. 1: the distance from the core. Cols. 2, 6, and 9: cluster stars for the regions in Col. 1. Column 4 gives the MF slopes (χ), derived for the low-mass and high-mass ranges. The masses of m_{evol}, m_{obs}, and m_{tot} are listed in Cols. 3, 7, and 10, respectively. The mass densities are given in Cols. 8 and 11.

TABLE 7 Mass function slopes (χ), relaxation time (t_{rlx} (Myr)), and evolutionary parameter (τ) of core and overall regions of the available clusters

	Core			Overall		
Cluster	χ	t_{rlx} (Myr)	τ_{core}	χ	t_{rlx} (Myr)	$\tau_{overall}$
NGC 436	−1.46 ± 0.47	0.46 ± 0.12	869.57 ± 314.19	0.86 ± 0.29	63.95 ± 38.60	6.25 ± 4.08
King 5	−3.06 ± 0.96	0.58 ± 0.11	1724.14 ± 475.22	1.80 ± 0.49	215.00 ± 148.09	4.65 ± 3.34
NGC 1513	1.12 ± 0.24	10.21 ± 6.40	9.79 ± 6.44	1.90 ± 0.12	175.88 ± 118.13	0.57 ± 0.40
Be 15	—	—	—	−1.54 ± 1.15	5.05 ± 2.78	99.01 ± 57.99
NGC 1907	−0.76 ± 0.40	1.71 ± 0.43	233.92 ± 82.95	0.00 ± 0.23	—	—
NGC 2112	−1.28 ± 0.51	3.28 ± 3.59	609.76 ± 673.63	0.50 ± 0.42	126.22 ± 78.13	15.85 ± 10.10
NGC 2158	−4.24 ± 1.00	5.05 ± 0.16	495.05 ± 61.44	−1.55 ± 0.71	—	—
Koposov 53	−3.96 ± 3.40	—	—	0.93 ± 0.81	15.51 ± 11.41	64.47 ± 47.86
NGC 2194	0.38 ± 0.42	13.15 ± 7.87	60.84 ± 39.46	2.52 ± 0.37	456.55 ± 311.22	1.75 ± 1.27
NGC 2192	−2.78 ± 0.96	0.36 ± 0.10	3611.11 ± 1040.84	± 3.12 ± 0.43	7.23 ± 0.85	179.81 ± 25.26
NGC 2243	—	—	—	2.09 ± 1.01	826.05 ± 654.27	2.42 ± 1.93
Trumpler 5	0.42 ± 0.75	1195.27 ± 869.82	2.51 ± 1.84	1.32 ± 1.18	3804.93 ± 2817.13	0.79 ± 0.59
Col 110	−2.58 ± 0.21	29.78 ± 4.37	100.74 ± 16.24	−2.84 ± 0.57	100.01 ± 22.83	30.00 ± 7.13
NGC 2262	−1.49 ± 0.80	0.43 ± 0.15	3023.26 ± 1079.96	1.01 ± 0.44	186.81 ± 126.13	6.96 ± 4.73
NGC 2286	1.30 ± 0.50	5.97 ± 4.26	167.50 ± 124.13	1.45 ± 0.30	99.95 ± 65.65	10.01 ± 6.87
NGC 2309	−1.52 ± 1.03	0.35 ± 0.07	1428.57 ± 404.06	−0.89 ± 0.60	—	—
Haffner 8	1.28 ± 0.77	5.50 ± 4.79	181.82 ± 159.39	1.82 ± 0.59	101.14 ± 68.47	9.89 ± 6.77
Mel 71	0.30 ± 1.04	—	—	1.29 ± 0.40	146.55 ± 99.37	10.24 ± 7.08
NGC 2506	4.11 ± 1.63	56.00 ± 49.28	35.71 ± 31.88	0.97 ± 0.63	822.94 ± 594.95	2.43 ± 1.79
Pismis 3	−1.60 ± 0.84	10.42 ± 2.03	307.10 ± 62.83	1.71 ± 0.49	1348.20 ± 939.15	2.37 ± 1.66
Ru 96	4.58 ± 0.98	17.70 ± 15.06	56.50 ± 48.40	4.55 ± 0.65	57.49 ± 40.92	17.39 ± 12.50
Trumpler 20	−1.07 ± 0.50	12.85 ± 17.60	116.73 ± 164.55	2.06 ± 0.68	2272.78 ± 1663.64	0.66 ± 0.53
Pismis 19	−2.42 ± 1.07	0.45 ± 0.10	1777.78 ± 453.27	1.18 ± 0.38	402.04 ± 272.33	1.99 ± 1.37
NGC 6134	−0.95 ± 0.90	—	—	−0.83 ± 1.11	—	—
IC 4651	−2.78 ± 0.75	1.09 ± 0.06	2293.58 ± 302.81	−0.60 ± 0.41	—	—
NGC 6802	−0.46 ± 0.84	—	—	1.66 ± 0.24	232.20 ± 156.40	3.88 ± 2.65
NGC 6819	−1.07 ± 0.55	—	—	0.47 ± 0.40	680.42 ± 429.71	3.67 ± 2.43
Be 89	0.18 ± 0.66	—	—	1.64 ± 0.93	312.83 ± 220.34	6.39 ± 4.78
NGC 6939	−2.17 ± 0.66	1.42 ± 0.07	1408.45 ± 222.38	0.84 ± 0.46	—	—
NGC 7142	−1.97 ± 1.44	—	—	−1.06 ± 0.56	—	—
NGC 7789	−0.42 ± 0.45	—	—	0.79 ± 0.65	5471.49 ± 3972.27	0.33 ± 0.24

sample size. The relation between R_{RDP} and R_{core} found by us is quite similar to that given by Camargo et al. (2010). However, analogous functions were found by other authors (Bica & Bonatto 2005; Bukowiecki et al. 2011; Maciejewski & Niedzielski 2007; Nilakshi et al. 2002; Sharma et al. 2006).

7.2 | Relations of cluster dimensions to the distance and age

The relations of R_{RDP} and R_{core} with d (kpc) are apparently linear, as displayed in Figure 15a,b. The linear best fits to the data (solid lines) are the following: $R_{RDP} = (2.67 \pm 0.27)\ d$ (kpc)

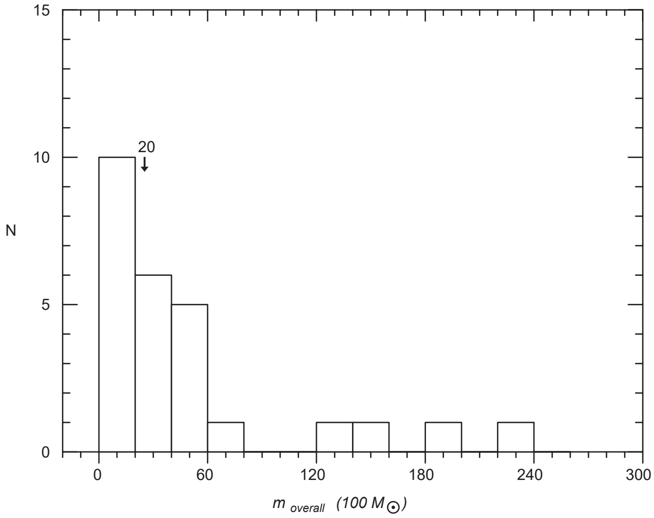

FIGURE 13 Overall mass distribution of 26 OCs

($CC = 0.84$) and $R_{\rm core} = (0.50 \pm 0.07)\ d$ (kpc) ($CC = 0.76$), respectively. Given a couple of deviants, the sizes ($R_{\rm RDP}$ and $R_{\rm core}$) increase on average with the distance from the sun. Similar trends were also obtained by Lynga (1982); van den Berg et al. (1991); Tadross et al. (2002); Bonatto & Bica (2010), and Bukowiecki et al. (2011).

The relations of $|z|$ and $R_{\rm GC}$ as a function of age and $R_{\rm RDP}$, respectively, are presented in Figure 16a,b. Younger and older clusters than 1 Gyr in panels (a) and (b) lie inside/outside the solar circle. No cluster with $R_{\rm RDP} > 8$ pc is seen in panel (a). OCs with age ≥ 1 Gyr in panel (b) do not show any dependence of $R_{\rm GC}$ and $R_{\rm RDP}$. The OCs NGC 2243 and NGC 2192 with $|z| > 800$ pc outside the solar circle in panels (b) and (c), where GMCs are scarce, might have been moved to outer parts of the galactic radii via tidal interactions with the disk and the galactic bulge, as well as collisions with GMCs. Alternatively, they may have been formed from molecular clouds at these distances. Note that Schilbach et al. (2006) have also detected large and small clusters outside the solar circle. From panel (b), we note that most of large/small OCs inside or outside the solar circle are located near the galactic plane ($|z| < 300$ pc) and the OCs inside the solar circle seem to survive four or more rotations around the galactic center. Their survival can be explained as due to that against external shocks (Janes & Phelps 1994).

Old clusters with large dimensions inside the solar circle in panel (b) may have a primordial origin, or their sizes may have increased via expansion due to stellar mass black hole couples. For the relation $|z|$–age as a function of $R_\odot$ in Figure 16c, the OCs with age ≥ 1 Gyr reach higher z distances, whereas those with age <1 Gyr have $|z| < 300$ pc.

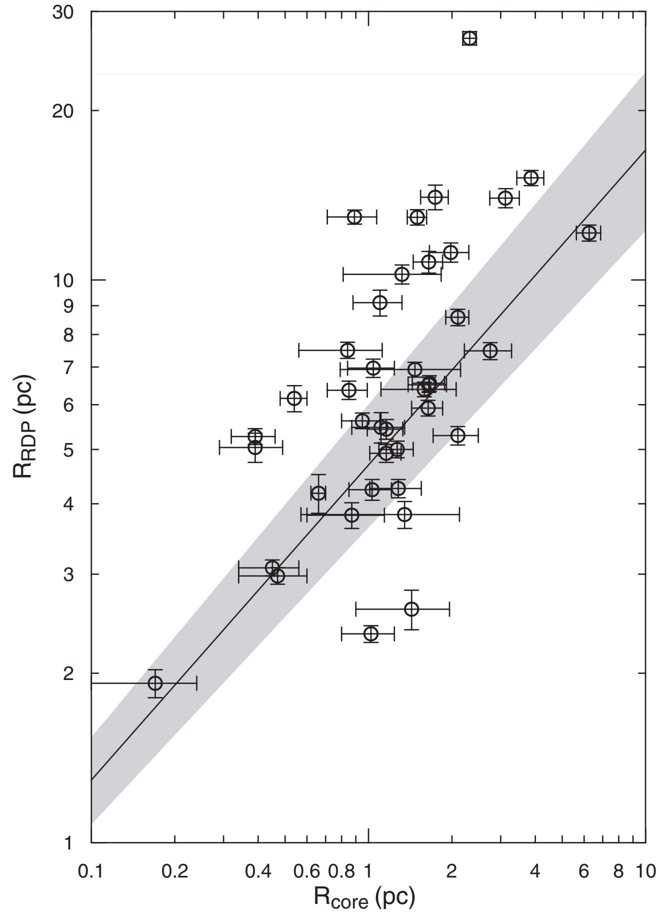

FIGURE 14 Relation of $R_{\rm RDP}$ versus $R_{\rm core}$ of 40 OCs. Empty circles show 40 OCs. Solid line and shaded area show the best fit and 1σ uncertainty, respectively

TABLE 8 Coefficients of the relation, $R_{\rm RDP} = a + bR_{\rm core}$, given in the literature between $R_{\rm core}$ and $R_{\rm RDP}$. The form of the relation of Camargo et al. (2010) is $R_{\rm RDP} = bR^{a}_{\rm core}$. CC and N in last two columns mean the correlation coefficient and data number, respectively

Author	*a*	*b*	*CC*	*N*
Nilakshi et al. (2002)	—	6	—	38
Bica & Bonatto (2005)	1.05	7.73	0.95	16
Sharma et al. (2006)	—	3.1	—	9
Maciejewski & Niedzielski (2007)	—	3.1	0.74	42
Camargo et al. (2010)	0.3	8.9	—	50
Bukowiecki et al. (2011)	0.58	6.98	0.93	140

7.3 | Relations of $R_{\rm RDP}$ versus age and $R_{\rm core}$ versus age

The relations of $R_{\rm core}$ − age and $R_{\rm RDP}$ − age are shown in Figure 17a,b. In the figure, the filled circles and empty triangles show 16 OCs with $m_{\rm overall} \geq 2{,}000\,M_\odot$ and 10 OCs with $m_{\rm overall} < 2{,}000\,M_\odot$, respectively. Fourteen OCs that have no mass determinations are marked by open squares. The relation in Figure 17a,b suggests a bifurcation that is seen at an age ≈ 1 Gyr. In the sense, in Figure 17, some clusters appear to expand ("A" arrow), while others contract ("B" arrow) with a bifurcation occurring at about 1 Gyr. Mackey et al. (2008) observed the bifurcation at ≈500–600 Myr (shown with "C" in the panels of Figure 17). This kind of relations in the panels were also observed by Bonatto & Bica (2007a); Maciejewski & Niedzielski (2007), and Camargo et al. (2010) from their OC samples.

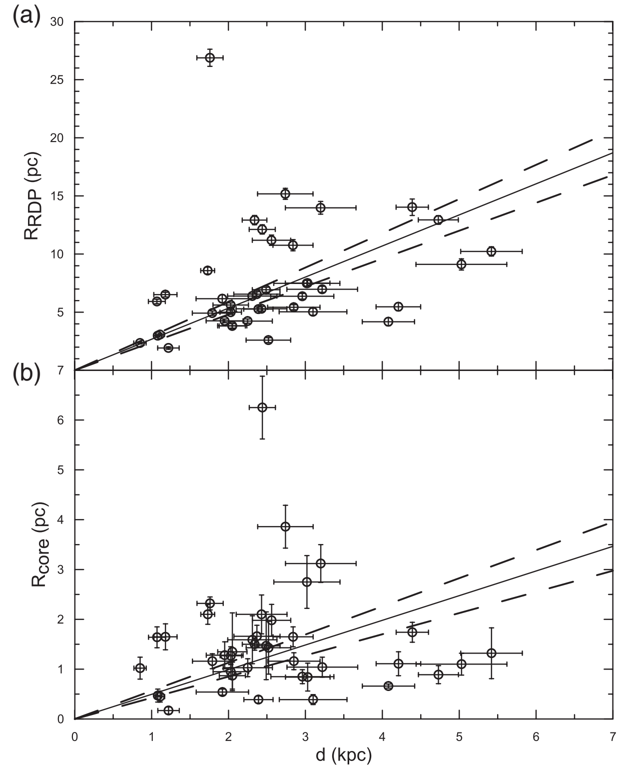

FIGURE 15 Relations of $R_{\rm RDP}$ versus d (kpc) (panel a), $R_{\rm core}$ versus d (kpc) (panel b). Solid and dashed lines show the best fit and 1σ uncertainty, respectively

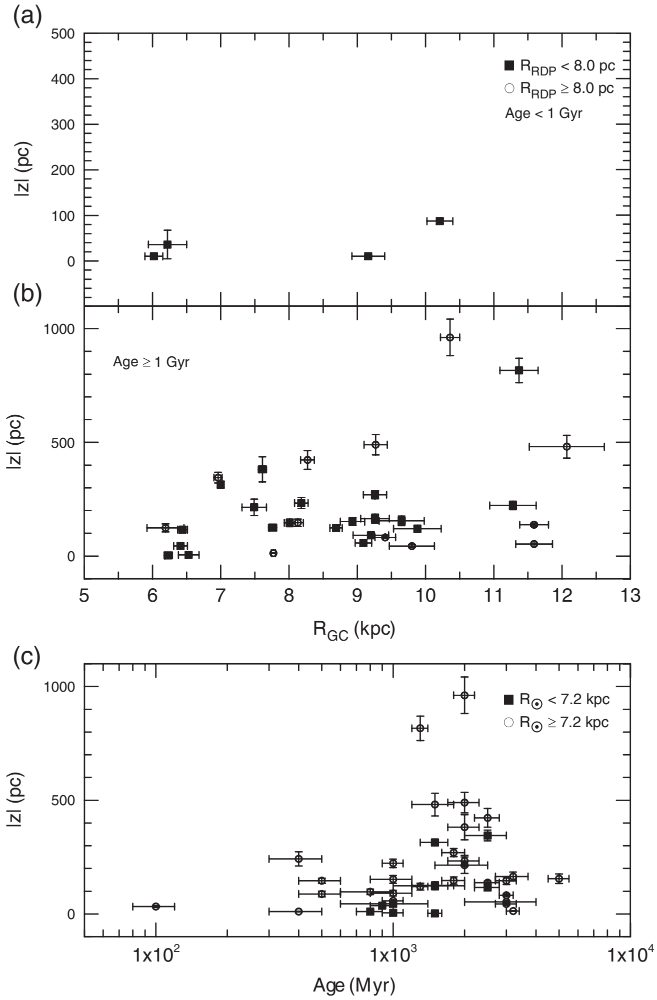

FIGURE 16 Relations of |z| versus $R_{\rm GC}$ in terms of $R_{\rm RDP}$ (panel a) and age (Myr) (panel b). Filled squares and empty circles show the OCs with $R_{\rm RDP} < 8$ pc and $R_{\rm RDP} \geq 8$ pc, respectively. Relation of |z| – age as function of $R_\odot$ (panel c)

Mackey et al. (2008) argue that some clusters show the expanded cores due to stellar mass black holes (hereafter BHs), and others contract due to dynamical relaxation and core collapse. To be able to see the effect of BHs in our core radius versus age relation, the information of the OCs in regions of R2 and R4 in Figure 17a is given in Tables 9 and 10. We call the regions in Figure 17 as R1, R2, R3, and R4. $N_{\rm bh}$ in Tables 9 and 10 means the estimated number of stellar mass BHs. This value is estimated from the relation $N_{\rm bh} = 6 \times 10^{-4}\, N_{\rm star}$, given by Portegies Zwart & McMillan (2000). Here, $N_{\rm star}$ is the extrapolated number of stars in the OCs, and is given in Col. 9 of Table 6 for the overall regions of OCs. Because the extrapolated stellar number for NGC 2158 is not available (Col. 9 of Table 6; Supporting Information), the number of BHs could be estimated from the relation $N_{\rm bh} \approx 0.002\ M_{\rm cluster}$ given by Portegies Zwart & McMillan (2000). The BH numbers of seven OCs in the regions R2 and R4 in Figure 17a cannot be estimated because their extrapolated star numbers or overall masses are not available (see Col. 9 of Table 6; Supporting Information).

7.4 | Relations of $R_{\rm RDP}$ and $R_{\rm core}$ with $R_{\rm GC}$

The relations of the structural parameters ($R_{\rm RDP}$ and $R_{\rm core}$) with their galactocentric distance $R_{\rm GC}$ of the 40 OCs as a function of the ages are plotted in Figure 18a,b. The large and small sized clusters in Fig 18a occupy the inner and the outer galactic radii. Two OCs with $R_{\rm RDP} < 7$ pc and age ≤ 1 Gyr in Figure 18a are located inside the galactic radius. Such OCs with these sizes and ages are also seen in Schilbach et al. (2006; fig. 3c). The relation between $R_{\rm RDP}$ and $R_{\rm GC}$ is the following: $R_{\rm RDP} = (0.98 \pm 0.25) R_{\rm GC} + (-3.07 \pm 2.03)$, with a correlation coefficient of 0.53 (Figure 18a). Our result shows that there is no strong dependence of $R_{\rm RDP}$ on $R_{\rm GC}$. However, Lynga (1982); Tadross et al. (2002), and Camargo et al. (2009, 2010) mention a correlation from their OC samples.

7.5 | Relations of $m_{\rm overall}$ with $R_{\rm RDP}$, $R_{\rm core}$, age, and $R_{\rm GC}$

Figure 19a,b, respectively, show the relations of $m_{\rm overall}$ versus $R_{\rm RDP}$ and $m_{\rm overall}$ versus $R_{\rm core}$ as a function of age of 26 of our 40 OCs. The relations to fit $m_{\rm overall}$ with $R_{\rm RDP}$ and with $R_{\rm core}$ are $\ln m_{\rm overall} = (1.57 \pm 0.42)\ \ln R_{\rm RDP} + (0.01 \pm 0.02)$ ($CC = 0.60$) and $\ln m_{\rm overall} = (1.14 \pm 0.37)\ \ln R_{\rm core} + (2.81 \pm 0.26)$ ($CC = 0.53$), respectively. These correlations between size and mass of the clusters are in concordance with the mass versus radius relation for massive OCs with age > 100 Myr (Camargo et al. 2010; Portegies Zwart et al. 2010)). In Figure 20a,b, the relations of $m_{\rm overall}$ with $R_{\rm GC}$ and of $m_{\rm overall}$ with age of 26 of our 40 OCs are

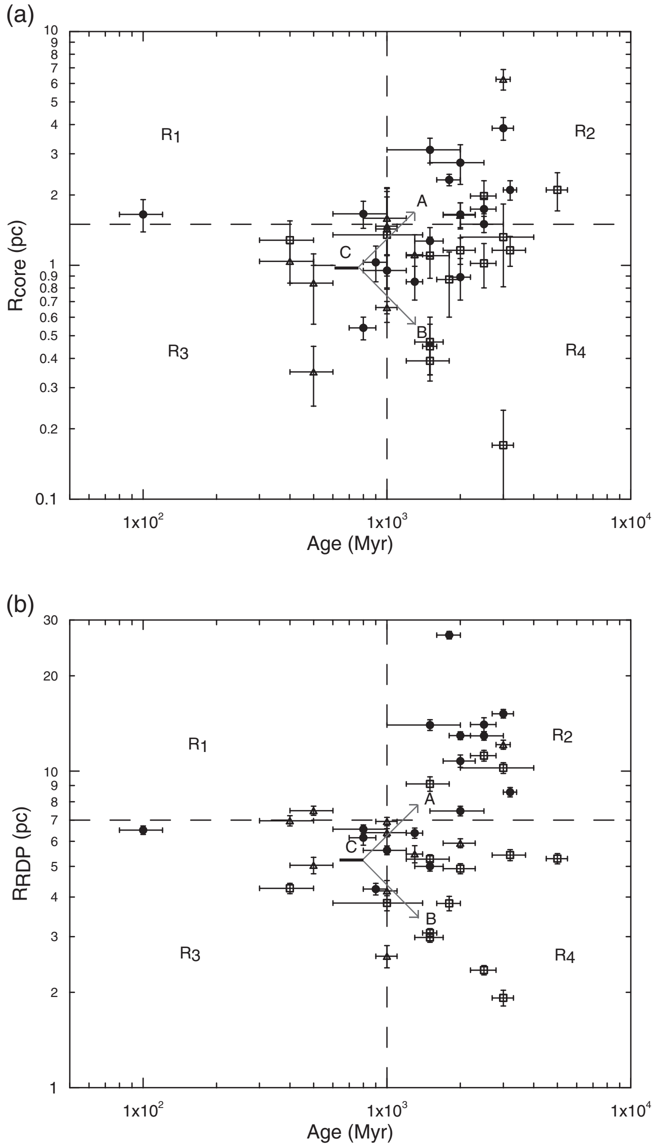

FIGURE 17 Relations of age versus $R_{\rm RDP}$ (panel a) and age versus $R_{\rm core}$ (panel b). Filled circles and empty triangles show 16 OCs with $m_{\rm overall} \geq 20\,M_\odot$ and 10 OCs with $m_{\rm overall} < 20\,M_\odot$, respectively. 14 OCs which have no mass determinations are marked by open squares. R1, R2, R3, and R4 mean the regions

shown. As is seen from Figure 20a that massive and less massive OCs than $m_{\rm overall} = 2{,}000\,M_\odot$ are located indistinctly inside or outside of the solar circle.

7.6 | Relations between MF slopes, age, $R_{\rm RDP}$, $R_{\rm GC}$, and the mass density

The relation of $\chi_{\rm overall}$ with $\chi_{\rm core}$ of 29 OCs is shown in Figure 21. The fit which is applied to the data is $\chi_{\rm overall} = (0.47 \pm 0.12)\chi_{\rm core} + (1.10 \pm 0.26)$, with a moderate $CC = 0.60$. The OCs with flat/steep positive overall MF slopes for $\chi_{\rm core} < 0$ in Figure 21 show signs of a mild to large-scale mass segregation, whereas the OCs with negative overall MF slopes for $\chi_{\rm core} < 0$ indicate an advanced dynamical evolution. These MF slopes of $\chi_{\rm core} < 0$ in Figure 21

TABLE 9 Age, dimensions, and mass (Cols. 2–5) for OCs that show the core shrinkage in Figure 17a. The number of black holes ($N_{\rm bh}$) is listed in last column

Cluster	Age (Myr)	$R_{\rm RDP}$ (pc)	$R_{\rm core}$ (pc)	$m_{\rm overall}$ ($100\,m_\odot$)	$N_{\rm bh}$
King 5	1,000	5.62	0.95	30.00	6
Koposov 53	1,000	4.18	0.66	2.37	0
NGC 2192	1,300	5.47	1.11	2.27	0
NGC 2243	2,000	12.94	0.89	51.70	10
NGC 2262	1,300	6.37	0.85	24.10	5
Haffner 8	1,000	6.93	1.47	9.85	2
Mel 71	1,500	5.00	1.27	21.80	4
Ru 96	1,000	2.60	1.43	15.80	3

TABLE 10 Age, dimensions, and mass (Cols. 2–5) for OCs that show the core shrinkage in Figure 17a. The number of black holes ($N_{\rm bh}$) is listed in last column

Cluster	Age (Myr)	$R_{\rm RDP}$ (pc)	$R_{\rm core}$ (pc)	$m_{\rm overall}$ ($100\,m_\odot$)	$N_{\rm bh}$
NGC 2112	2,000	5.92	1.64	18.10	4
NGC 2158	2,500	14.03	1.74	33.40	7
Trumpler 5	3,000	15.18	3.86	223.0	45
Col 110	3,000	12.12	6.25	16.50	3
NGC 2286	1,000	6.39	1.59	11.10	2
NGC 2506	2,000	10.76	1.65	65.80	13
Pismis 3	3,200	8.58	2.10	133.00	27
Trumpler 20	1,500	13.98	3.12	150.00	30
NGC 6819	2,500	12.92	1.50	49.10	10
Be 89	2,000	7.48	2.75	32.00	6
NGC 7789	1,800	26.88	2.32	194.00	39

can be explained by the external dynamical effects such as tidal stripping by tidal interactions (in the form of shocks) due to disk and bulge crossings, as well as by encounters with GMCs.

The relations of age versus $\chi_{\rm overall}$ of 31 OCs and age versus $\chi_{\rm core}$ of 29 OCs of our sample are shown in Figure 22a,b, respectively. The age dependence of the overall and core MF slopes has been parameterized by the linear decay function (shown as dashed curve) $\chi(t) = \chi_0 - t/t_{\rm f}$, where χ_0 represents the MF slope in the early phases and $t_{\rm f}$ is the flattening timescale. For the overall MF, we derive $\chi_0 = 1.68 \pm 0.30$ and $t_{\rm f} = 1{,}569 \pm 600$ Myr ($CC = 0.44$), the core values $\chi_0 = 0.74 \pm 0.39$, and $t_{\rm f} = 1{,}006 \pm 206$ Myr ($CC = 0.68$). Within the expected uncertainties, the overall MF values are quite close to $\chi_0 = 1.30 \pm 0.30$ of Kroupa (2001) and $\chi_0 = 1.35$ of Salpeter (1955).

The relations of $m_{\rm overall}$ with the slope $\chi_{\rm overall}$ of 26 OCs and $m_{\rm core}$ with $\chi_{\rm core}$ of 24 OCs are presented in Figure 23a,b, respectively. In Figure 23a, most of the OCs of with positive overall slopes are mass-rich and present little or no sign of mass segregation. For the relation of $m_{\rm core}$ with $\chi_{\rm core}$ displayed in Figure 23b, most of OCs with $m_{\rm core} < 1{,}000\,m_\odot$ have negative core MF slopes, implying mass segregation effects at a larger scale.

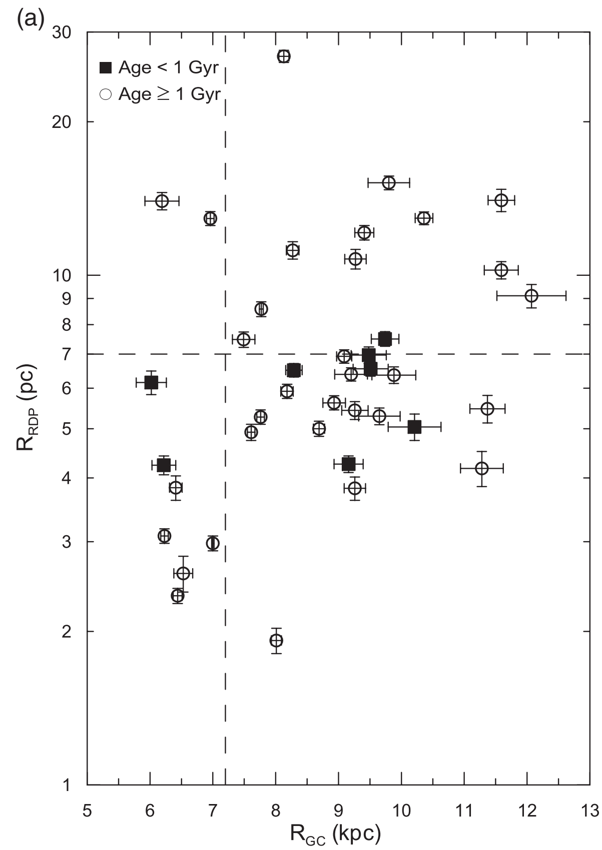

FIGURE 18 Relations of R_{GC} versus R_{RDP} (panel a) and R_{GC} versus R_{core} (panel b). Filled squares and open circles denote the OCs with age < 1 Gyr and age ≥ 1 Gyr, respectively

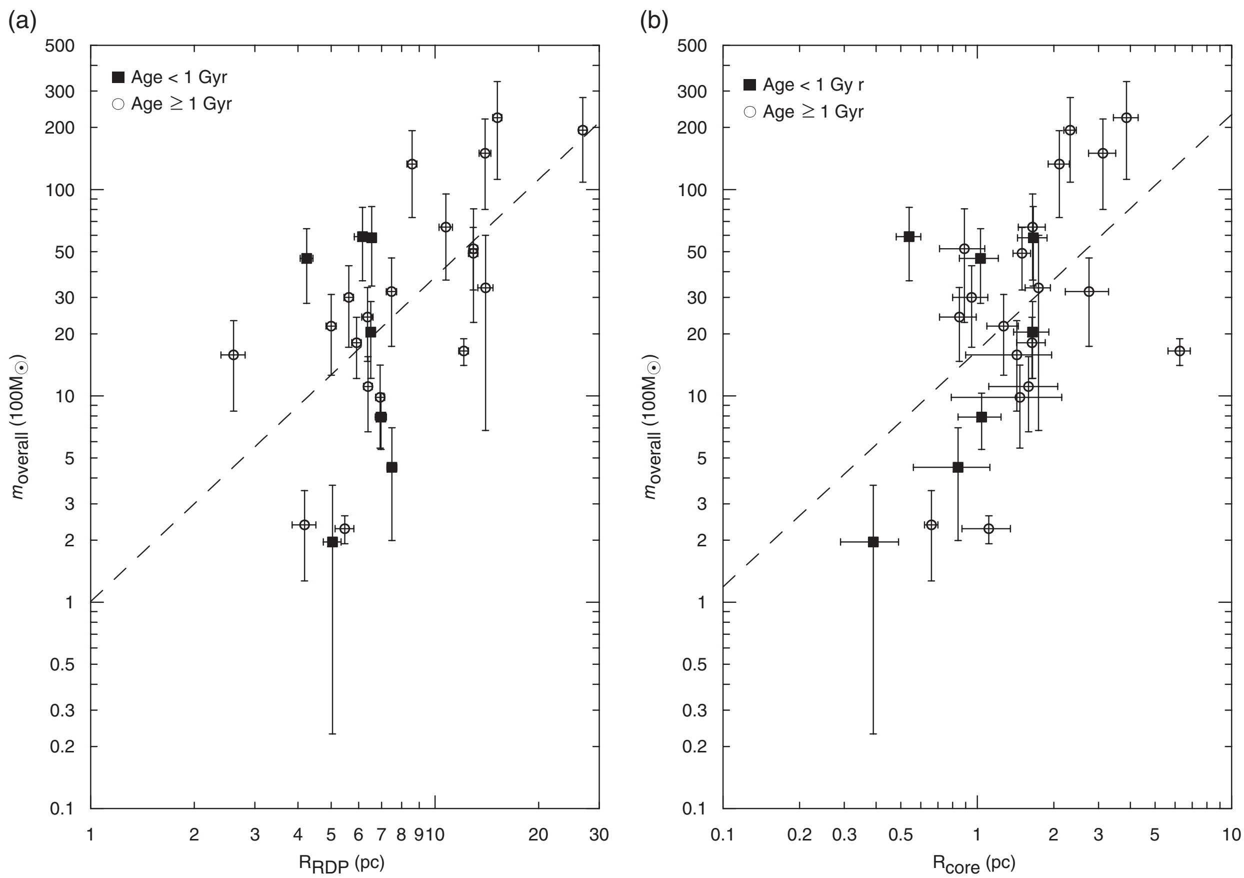

FIGURE 19 Relations of R_{RDP} versus $m_{overall}$ (panel a) and R_{core} versus $m_{overall}$ (panel b) of 26 OCs. Filled squares and open circles represent the OCs with age < 1 Gyr and age ≥ 1 Gyr. Dashed lines denote the best fits

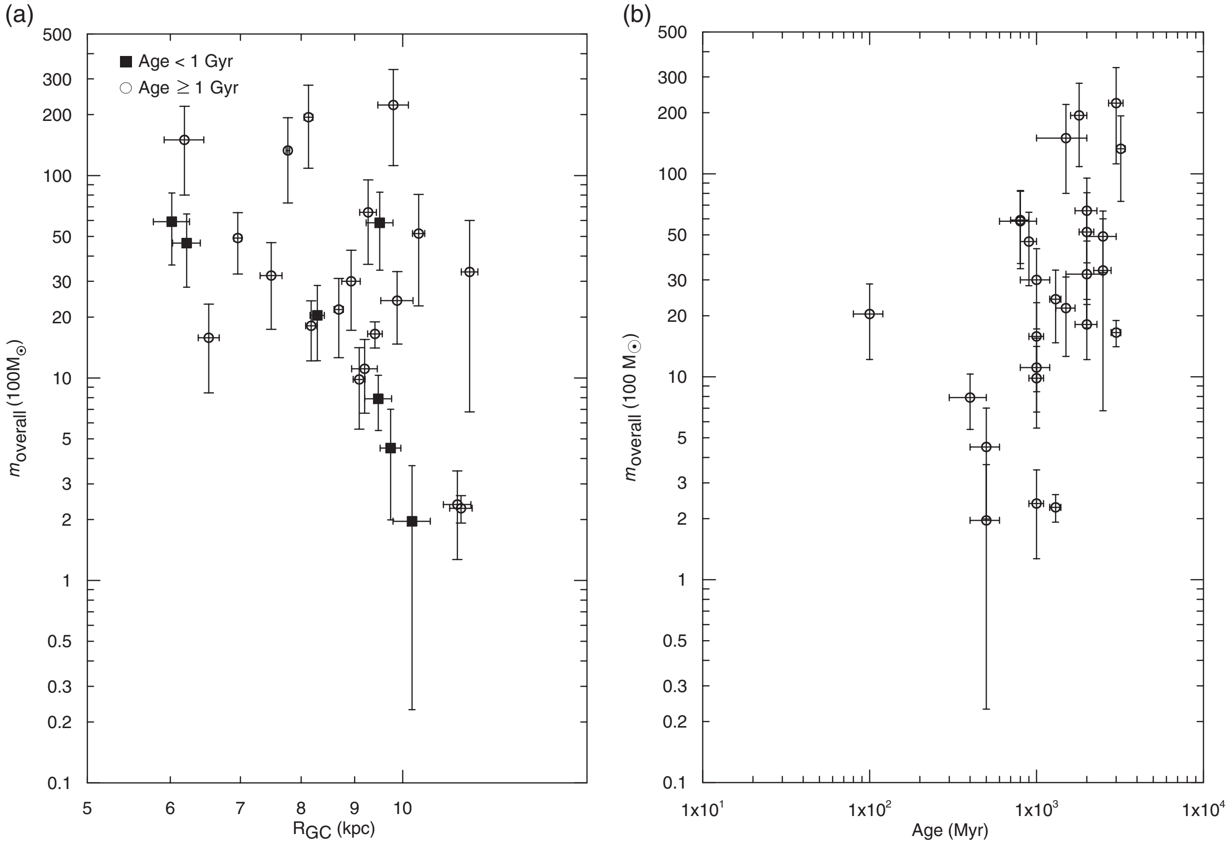

FIGURE 20 Relations of R_{GC} versus m_{overall} (panel a) and age versus m_{overall} (panel b) of 26 OCs

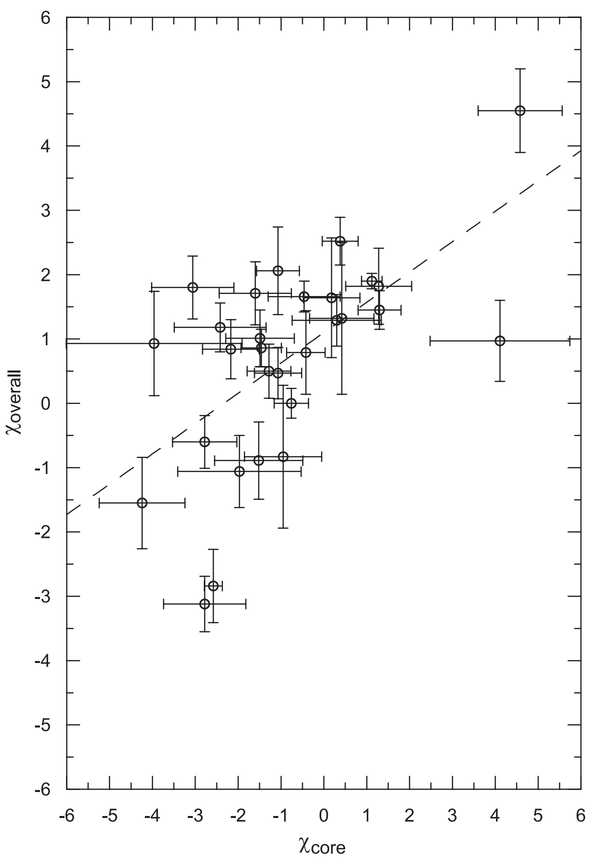

FIGURE 21 Relation of χ_{core} versus χ_{overall} of 29 OCs. Dashed line shows the best fit

In the relations of R_{RDP} with χ_{overall} and R_{RDP} with χ_{core} for 31 and 29 OCs of our sample, respectively, given in Figure 24a,b, the OCs with larger or smaller dimensions than $R_{\mathrm{RDP}} = 7$ pc have a positive or negative sloped overall and core MFs, respectively.

From the relations between R_{GC} and χ_{overall} of 31 OCs and between R_{GC} and χ_{core} of 29 OCs shown in Figure 25a,b, respectively, apparently the MF slopes are not correlated with R_{GC} or age.

The cluster mass density ρ ($m_{\odot}\,\mathrm{pc}^{-3}$) is plotted in Figure 26a,b as a function of χ_{overall} for 26 OCs and χ_{core} for 24 OCs, respectively. In panel (a), the mass densities of the OCs having $\chi_{\mathrm{overall}} < 0$ are low compared to those of the OCs with $\chi_{\mathrm{overall}} > 0$. This indicates that low-mass stars of OCs with negative MF slopes are significantly lost as a result of external dynamical processes. From panel (b), one can see that χ_{core} and ρ_{core} are not correlated.

7.7 | Relation between the MF slope and the evolutionary parameter and a comparison to Kroupa's IMF

From MF slopes and evolutionary parameters of the overall and the core of the OCs given in Table 7, the relations of τ_{overall} with χ_{overall} of 24 OCs and of τ_{core} with χ_{core} of 21 OCs are plotted in Figure 27a,b. The dashed curve in the figure shows the fit $\chi(\tau) = \chi_0 - \chi_1 e^{-(\tau_0/\tau)}$. As seen in panels (a) and (b) of Figure 27, the overall

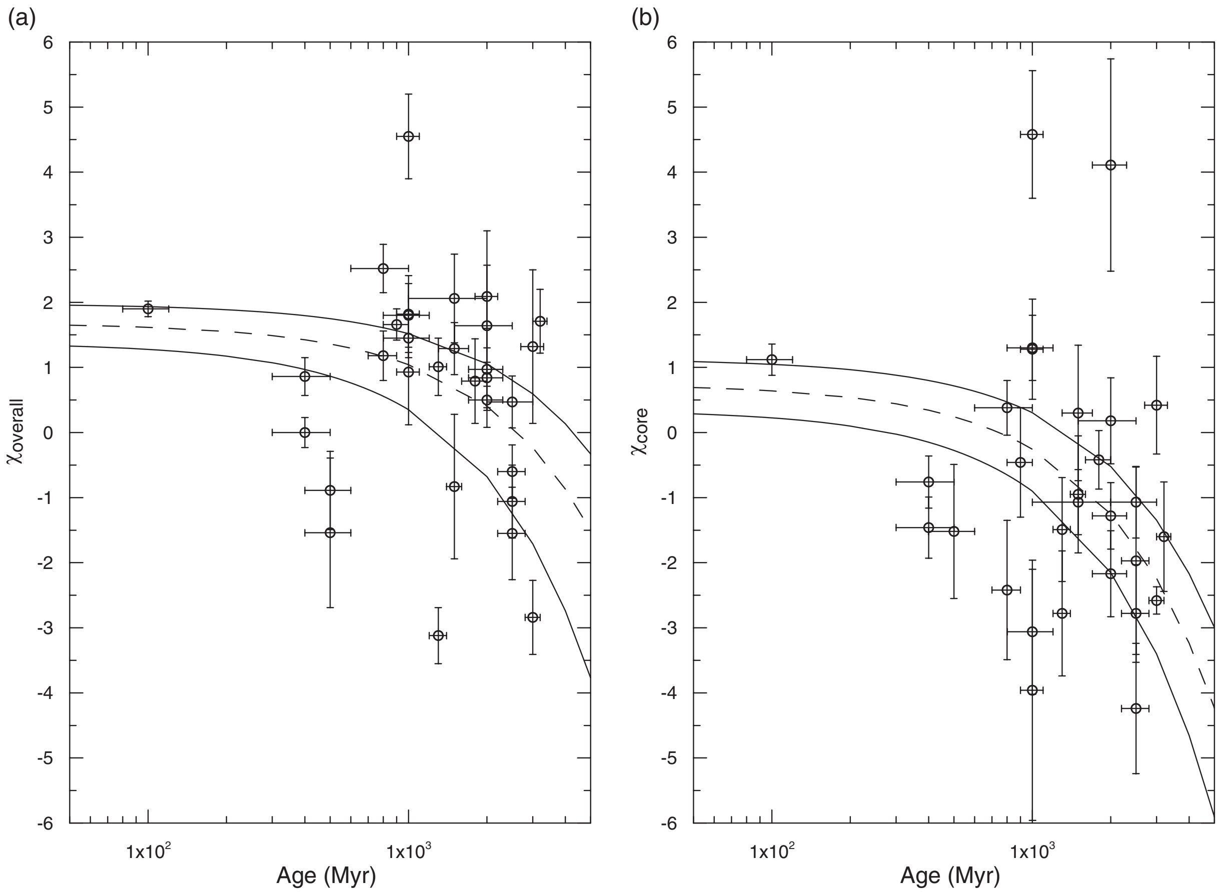

FIGURE 22 Relations of age versus $\chi_{\rm overall}$ (31 OCs, panel a) and age versus $\chi_{\rm core}$ (29 OCs, panel b). Dashed and solid lines show the best fit and 1σ uncertainty, respectively

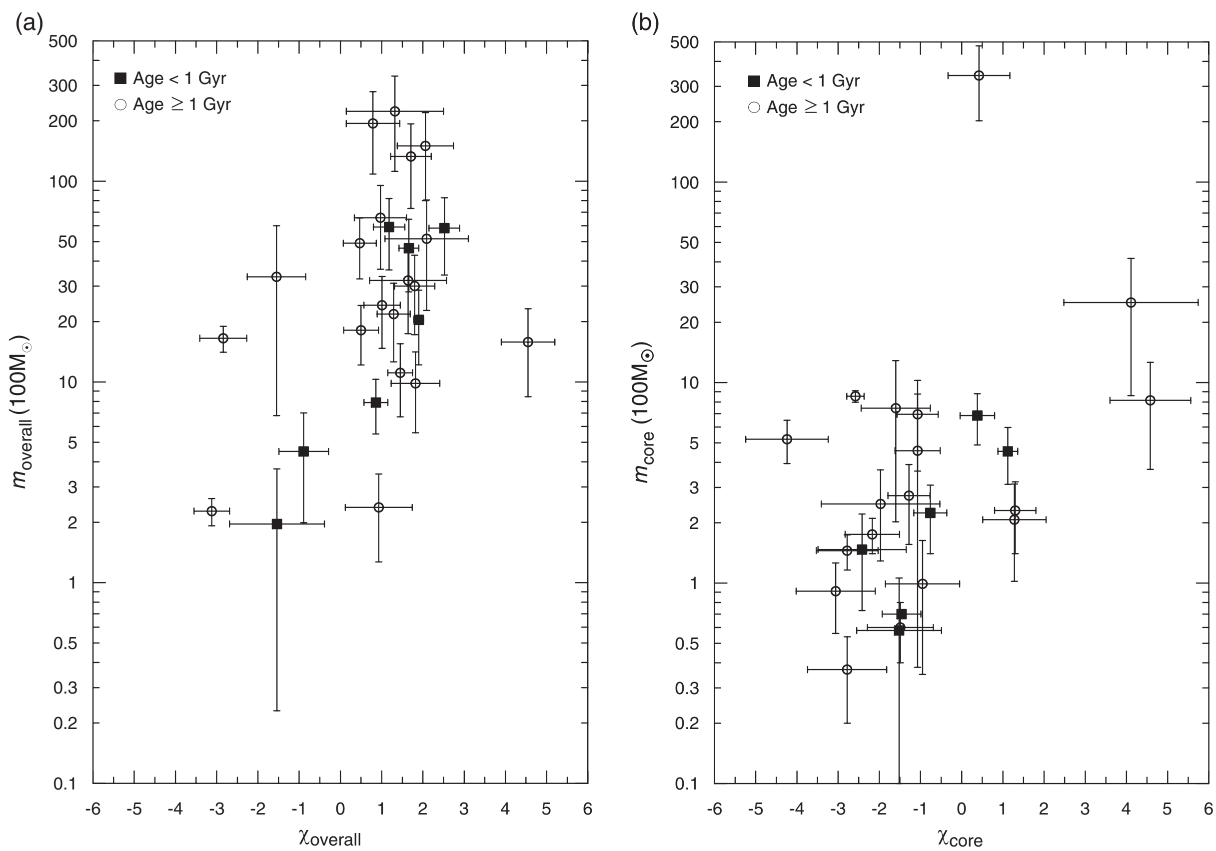

FIGURE 23 Relations of $m_{\rm overall}$ versus $\chi_{\rm overall}$ (panel a) of 26 OCs and $m_{\rm core}$ versus $\chi_{\rm core}$ (panel b) of 24 OCs, respectively

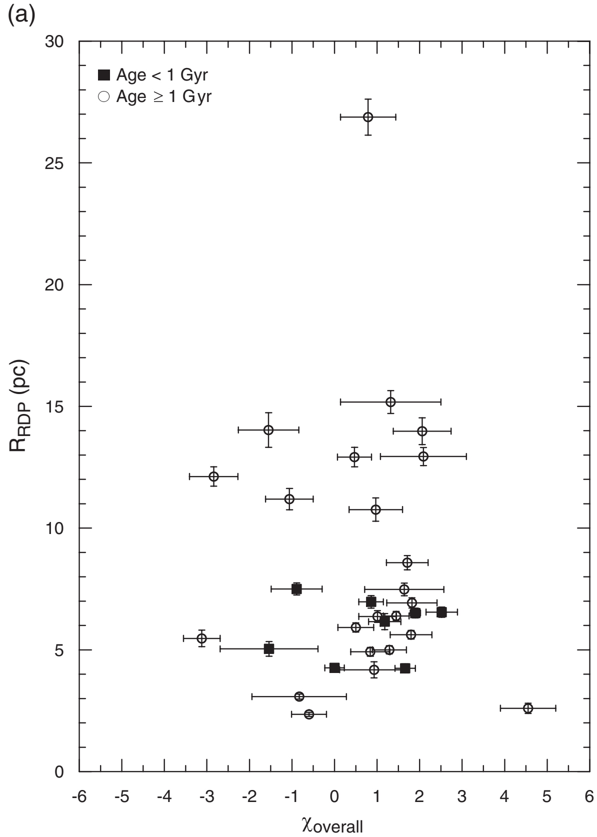

FIGURE 24 Relations of χ_{overall} versus R_{RDP} (panel a) of 31 OCs and χ_{core} versus R_{RDP} (panel b) of 29 OCs. Filled squares and open circles denote clusters with age < 1 Gyr and age ≥ 1 Gyr, respectively

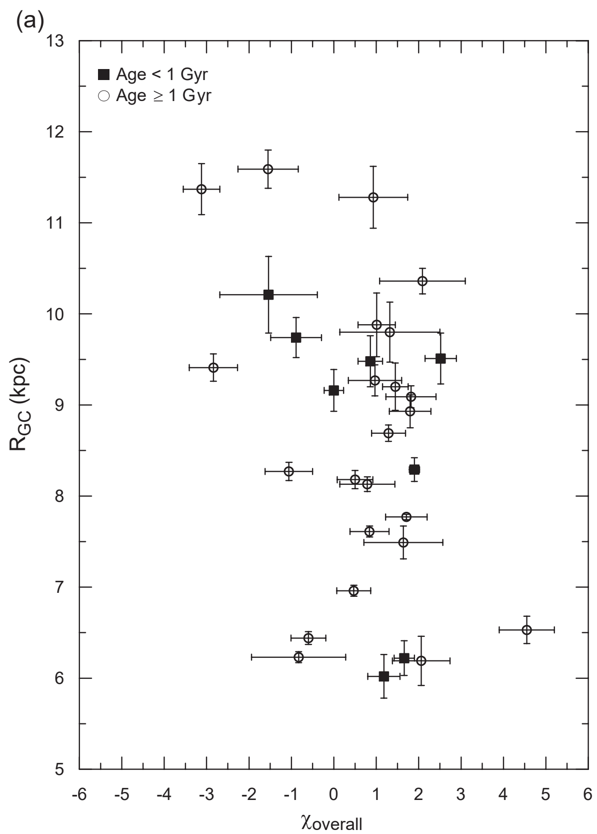

FIGURE 25 Relations of χ_{overall} versus R_{GC} (panel a) of 31 OCs and χ_{core} versus R_{GC} (panel b) of 29 OCs, respectively

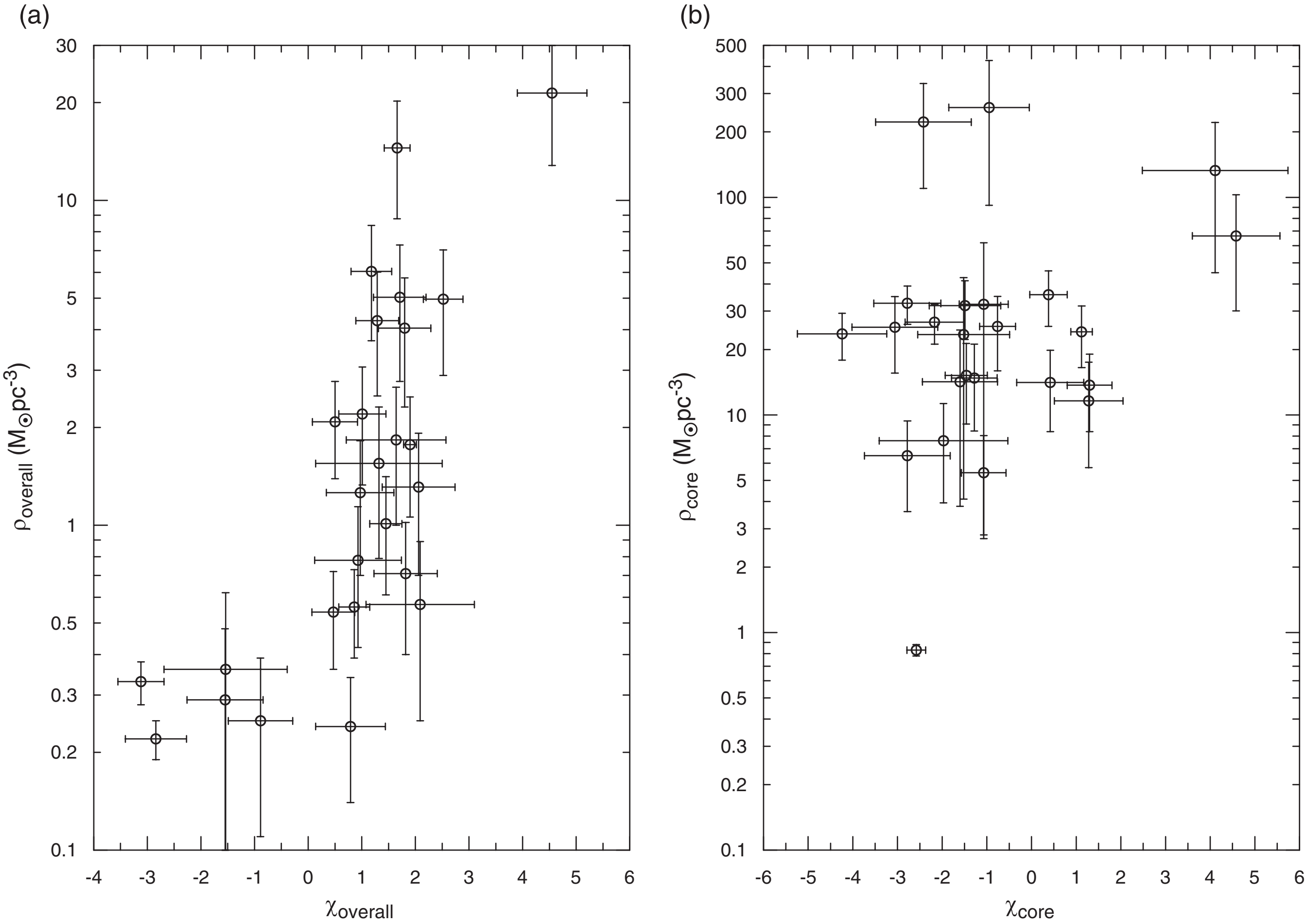

FIGURE 26 Relations of $\chi_{overall}$ versus $\rho_{overall}$ (panel a) of 26 OCs and χ_{core} versus ρ_{core} (panel b) of 24 OCs, respectively

and core MF slopes undergo an exponential decay with τ. Here, χ_0 and χ_1 mean MF slopes at birth and in the advanced stage, respectively. For the overall MF slope, we derive $\chi_0 = 1.67 \pm 0.18$ and $\tau_0 = 29.92 \pm 12.29$ ($CC = 0.77$), the core values $\chi_0 = 1.19 \pm 0.89$ and $\tau_0 = 31.62 \pm 34.79$ ($CC = 0.64$). Similar relations were obtained by Bica et al. (2006b; fig. 8a,b) and Maciejewski & Niedzielski (2007; fig. 7b,d,e).

8 | CONCLUSIONS

Our main conclusions can be summarized as follows:

1. The astrophysical and structural parameters of 40 OCs have been derived from the filtered 2MASS (J, $J-H$) CMDs and the stellar RDPs. The field star decontamination technique was used for separating the cluster members. The astrophysical parameters (age, d, $E(B-V)$) of 40 OCs along with ages in the range 0.1–5.0 Gyr, at heliocentric distances 0.85–5.42 kpc, and with reddenings $0.03 \leq E(B-V) \leq 1.31$ are given in Table 3. Having combined the derived structural, mass and mass functions, relaxation, and evolutionary parameters with astrophysical parameters of 40 OCs, the dynamical evolution of these OCs was studied. The reduced final reddenings from the dust maps of SFD were compared with those of 40 OCs (Figure 9b). There are significant differences for 27 OCs between both $E(B-V)$ color excess values. For the rest, the $E(B-V)$ values of 13 OCs are quite close to those of SFD. Note that SFD maps are not reliable at regions $|b| < 5°$ due to contaminating sources and uncertainties in the dust temperatures (Gonzalez et al. 2012). Therefore, the SFD values resulting from line-of-sight integral through the Milky Way and with low spatial resolution normally have different reddening values for these relatively close (~1 kpc) star clusters.
2. The relation between R_{RDP} and R_{core} in Figure 14 is quite similar to that given by Camargo et al. (2010). The OCs in our sample that do not follow the relation are either intrinsically small or have been suffering from significant evaporation effects. The dimensions (R_{RDP} and R_{core}) in Figure 15a,b increase on average with the distance from the sun.
3. From Figure 17a and Tables 9 and 10, it is apparent that the sizes of core radii of the OCs are related to their respective BH numbers. The BH numbers of the OCs in region R2 of Figure 17a are generally larger than those of the OCs in the region of IV. Note that the BH numbers

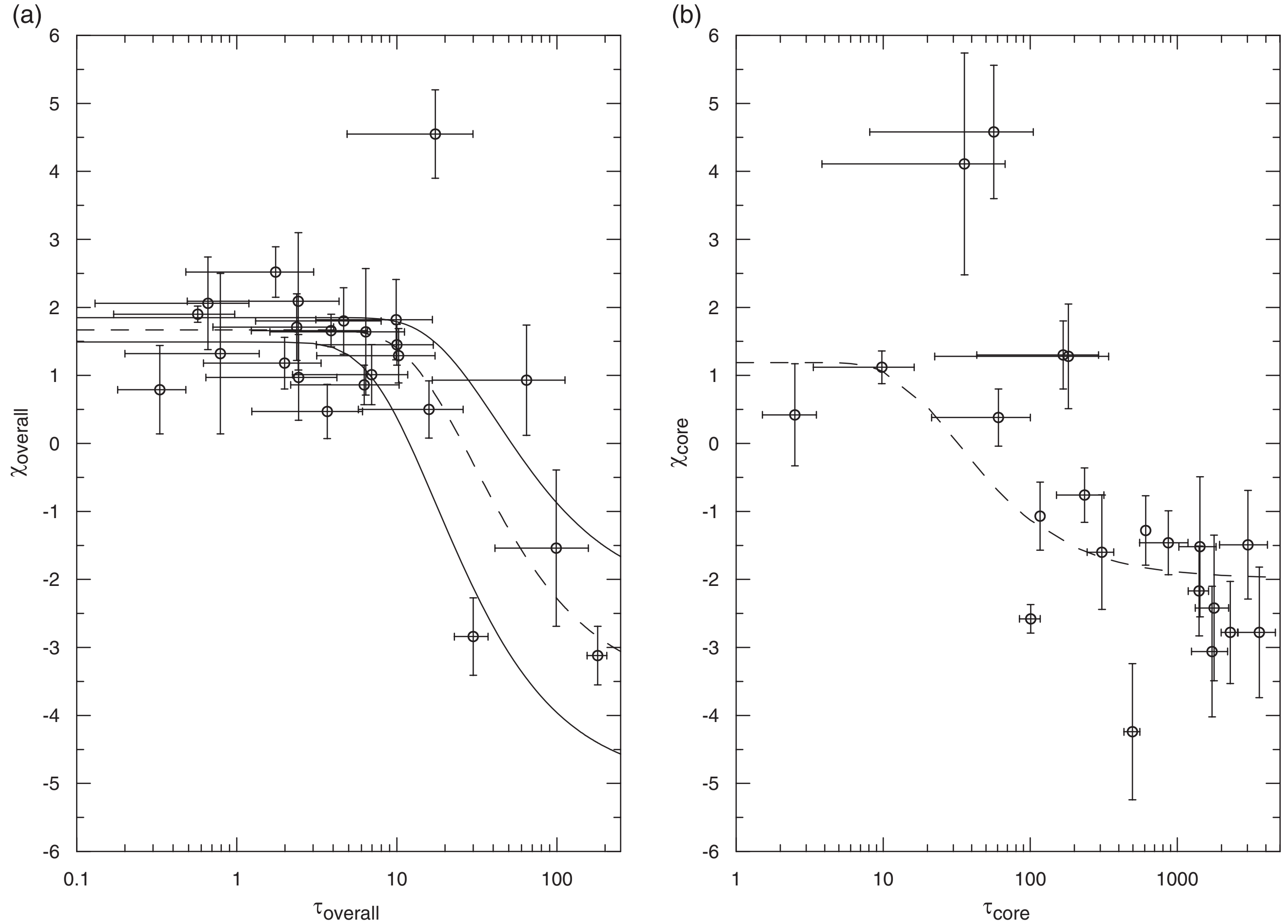

FIGURE 27 Relations of $\tau_{overall}$ versus $\chi_{overall}$ (panel a) of 24 OCs and τ_{core} versus χ_{core} (panel b) of 21 OCs. Dashed and solid lines show the best fit and 1σ uncertainty, respectively. In panel (b), 1σ uncertainty is not shown due to too large error of τ_{core}

of 6 out of 10 OCs in Table 10 are almost close to those of the OCs in Table 9. However, with almost similar BH numbers, these six OCs show shrinkage, whereas those in Table 9 indicate the expanded cores. For example, if the statement of Mackey et al. (2008) is correct, NGC 2243 with its 10 BHs would develop a large core. However, NGC 2243 has a small core value with $R_{core} = 0.89$ pc. In the sense, Col.110 OC has a few BHs showing an expanding core with $R_{core} = 6.25$ pc. The core sizes of NGC 7789 ($R_{core} = 2.32$ pc) and Be 89 ($R_{core} = 2.75$ pc) are quite close. But the BH numbers of the two OCs are very different. Therefore, the presence of BHs is not the only possible explanation for the bifurcation seen in Figure 17a,b. Alternatively, one should also consider the effect of the mass range of OCs. In other words, for clusters older than 1 Gyr, Figure 17 shows that massive OCs (filled circles) can be found in both regions R2 and R4. There are two low-mass OCs (open triangles) in the region R4 (Figure 17a). In this sense, the distribution of OCs in Figure 17 can be partly attributed to clusters with large radii retaining larger masses.

4. Mackey & Gilmore (2003) and Mackey et al. (2008) also argue that the expanded cores are the cause of growth of the limiting radii, and the shrinking cores lead to the contraction of the limiting radii. There are 32 OCs of our sample in the regions R2 and R4 in Figure 17a; 16 out of 19 OCs with $R_{core} < 1.5$ pc in the region R4 of Figure 17a have $R_{RDP} < 7$ pc; and 3 of 19 OCs have $R_{RDP} > 7$ pc. Similarly, 10 out of 13 OCs in the region R2 of Figure 17a with $R_{core} > 1.5$ pc have $R_{RDP} > 7$ pc, and 3 of them have $R_{RDP} < 7$ pc. Here, $R_{RDP} = 7$ pc means the separation into two groups of our sample (Figure 11a). These findings imply that the OCs with their core expanding could have small cluster limiting radii; in a similar manner, the OCs with shrinking cores could have large limiting cluster radii. Note that there are six OCs with incompatible cores and limiting radii in the regions R2 and R4 of Figure 17b. These six OCs are inconsistent with the arguments of Mackey & Gilmore (2003) and Mackey et al. (2008).
5. It is seen from Figure 18a,b that the OCs with $R_{RDP} < 3$ pc and $R_{core} < 0.6$ pc inside the solar circle are older than 1 Gyr. As they lost their stellar content, they shrunk in size and mass with time. Nevertheless, they seem to have survived against external shocks for a longer time, according to the simulations of Spitzer & Chevalier (1973). As one can see from Figure 18b, there is no strong dependence of R_{core} on R_{GC}.

6. As can be seen in Figure 19a,b, OCs with large dimensions are on average more massive. There does not seem to be an age dependence for the relations in the panels (a) and (b) of Figure 19. As can be seen from Figure 20a, massive and less massive OCs than $m_{\mathrm{overall}} = 2{,}000\,M_\odot$ are located indistinctly inside or outside of the solar circle. Less massive OCs that are located outside the solar circle appear to survive, because they are subjected to less external dynamical processes: The OCs inside the solar radius survive against the combined dynamical effects such as interactions with GMCs and tidal effects with the spiral arm and the galactic disk, which are quite efficient in the galactic center directions. As is seen in Figure 20b, less massive OCs older than 1 Gyr are scarcer since they are dissolved into the field; i.e., the more massive and older OCs (>1 Gyr) survive.

7. The OCs with flat/steep positive overall MF slopes for $\chi_{\mathrm{core}} < 0$ in Figure 21 show signs of a mild to large-scale mass segregation, whereas the OCs with negative overall MF slopes for $\chi_{\mathrm{core}} < 0$ indicate an advanced dynamical evolution. These MF slopes of $\chi_{\mathrm{core}} < 0$ in Figure 21 can be explained by the external dynamical effects such as tidal stripping by tidal interactions (in the form of shocks) due to disk and bulge crossings, as well as by encounters with GMCs.

8. Considering these MF slopes in Figure 22a,b, OCs are formed with flat core and Kroupa and Salpeter-like overall MFs, as stated by Bonatto & Bica (2006). As is seen from Figure 22, at the birth of a cluster, the core MF seems to be much flatter than the overall MF. Early core flattening may be partly linked to primordial processes associated with molecular cloud fragmentation. Within the expected uncertainties, the overall MF values are quite close to $\chi_0 = 1.30 \pm 0.30$ of Kroupa (2001) and $\chi_0 = 1.35$ of Salpeter (1955). However, our core MF values are smaller than those of Kroupa and Salpeter. As is seen from panels (a) and (b), except for few MF slopes, the overall and core MF slopes tend to be negative towards older ages, because of mild/large-scale mass segregation as well as the presence of GMCs and tidal effects from disk and bulge crossings as external processes.

9. Most of the OCs with positive overall slopes in Figure 23a are mass-rich and present little or no signs of mass segregation. Apparently, they retain their low-mass stars because they are strongly bounded to the clusters. The OCs with negative overall MF slopes in Figure 23a seem to be in the phase of more advanced dynamical evolution. In panels (a) and (b) of Figure 23, there is no indication of age dependence that is seen between the MF slopes and the core or overall masses. In panels (a) and (b) of Figure 23, the OCs with steep overall and core MF slopes present signs of larger scale mass segregation in the core or halo region. As expected, there are no indications of age dependence among the positive/negative MF slopes.

10. From Figure 27a, one sees that for $\tau > 30$, the overall MF slopes of the OCs are negative, with one exception. For $\tau < 30$, the overall MF slopes of the remaining OCs fall in the range $+0.5 < \chi_{\mathrm{overall}} < +2.5$. For $\tau > 30$, as a result of the loss of low-mass stars, χ_{overall} tends to be negative. As can be seen from panel (b), the core MF slopes for the majority of OCs tend to be negative after $\tau \approx 32$, with two exceptions. In panel (b), there are two OCs with flat slopes for $\tau < 32$. For $\tau > 32$, it is seen from panel (b) that the OCs with dynamically evolved cores reveal a sign of strong mass segregation.

From 11 OCs, Bonatto & Bica (2005) detected the significant flattening in MF slopes for $\tau_{\mathrm{core}} \leq 100$ and $\tau_{\mathrm{core}} \leq 7$, respectively. From their OCs, Maciejewski & Niedzielski (2007) give these values as $\tau_{\mathrm{core}} \leq 1{,}000$ and $\tau_{\mathrm{overall}} \leq 450$, respectively. Here we detect the flattening of MF slopes at $\tau_{\mathrm{core}} \leq 32$ and $\tau_{\mathrm{overall}} \leq 30$, respectively. However, these values are affected by the sample size with young and old OCs. Note that our sample also contains OCs with intermediate and old ages.

The overall MF slopes of 31 OCs with $m > 0.5\,M_\odot$ could have been compared with those given by Kroupa (2001) ($\chi = +1.3 \pm 0.3$). As compared to the uncertainties of our MF slopes (Col. 5; Table 7) and that (± 0.3) of Kroupa, the overall MF slopes of 14 out of 31 OCs are consistent with that of Kroupa (2001) ($\chi = +1.3 \pm 0.3$), which implies little or no dynamical evolution for these clusters. The remaining 17 OCs with MF slopes that depart from that of Kroupa (2001) show mild to large-scale mass segregation due to the dynamical evolution.

11. We do not make an effort to determine the binary fractions of our sample OCs. Sollima et al. (2010) give the complete fractions of binaries as 35–70%. They also give a minimum binary fraction, which is larger than 11% within the core of OCs. However, binaries of the OCs widen the main sequence of the OCs by as much as 0.75 mag, so theoretical isochrones are fitted to the mid-points of CMDs of the OCs rather than the faint or blue sides, as emphasized by Carney (2001). We have considered this issue for isochrone fitting to CMDs (see Section 4). Binaries are indeed an effective way of storing energy in a cluster. Nonprimordial binary formation, especially the close ones, requires many encounters of at least three stars, two of which end up having orbits around each other and the third one gets "ejected." So, depending on the binary fraction, a cluster can get dynamically swollen. As a consequence of the dynamical evolution in OCs, multiple systems tend to concentrate in central regions (Takahasi & Portegies Zwart 2000). As indicated by Bonatto et al. (2005), the main effect of a significant fraction of binaries in central parts of OCs is that the number of low-mass stars is underestimated with respect to the higher mass stars.

ACKNOWLEDGEMENTS

We thank the anonymous referee for her/his comments and suggestions on the manuscript. We also thank C. Chavarria for the correction of English in the text. This publication makes use of data products from the *Two Micron All Sky Survey*, which is a joint project of the University of Massachusetts and the Infrared Processing and Analysis Centre/California Institute of Technology, funded by the National Aeronautics and Space Administration and the National Science Foundation. This research has made use of the WEBDA database, operated at the Institute for Astronomy of the University of Vienna.

REFERENCES

Bahcall, J. N., & Soneira, R. M. 1980, *ApJ*, *238*, 17.
van den Berg, S., Morbey, C., & Pazder, J. 1991, *ApJ*, *375*, 594.
van den Bergh, S., & McClure, R. D. 1980, *A&A*, *88*, 360.
Bergond, G., Leon, S., & Guibert, J. 2001, *A&A*, *377*, 462.
Bica, E., & Bonatto, C. 2005, *A&A*, *443*, 465.
Bica, E., Bonatto, C., Barbuy, B., et al. 2006a, *A&A*, *450*, 105.
Bica, E., Bonatto, C., & Blumberg, R. 2006b, *A&A*, *460*, 83.
Binney, J., & Merrifield, M. 1998, *Galactic Astronomy*, Princeton University Press (Princeton, NJ). Princeton series in astrophysics.
Bonatto, C., & Bica, E. 2005, *A&A*, *437*, 483.
Bonatto, C., & Bica, E. 2006, *A&A*, *455*, 931.
Bonatto, C., & Bica, E. 2007a, *A&A*, *473*, 445.
Bonatto, C., & Bica, E. 2007b, *MNRAS*, *377*, 1301.
Bonatto, C., & Bica, E. 2008, *A&A*, *485*, 81.
Bonatto, C., & Bica, E. 2009a, *MNRAS*, *392*, 483.
Bonatto, C., & Bica, E. 2009b, *MNRAS*, *394*, 2127.
Bonatto, C., & Bica, E. 2009c, *MNRAS*, *397*, 1915.
Bonatto, C., & Bica, E. 2010, *A&A*, *521*, 74.
Bonatto, C., Bica, E., & Santos, J. F. C. Jr. 2005, *A&A*, *433*, 917.
Bonifacio, P., Monai, S., & Beers, T. C. 2000, *AJ*, *120*, 2065.
Bragaglia, A., Carretta, E., Gratton, R. G., et al. 2001, *AJ*, *121*, 327.
Bragaglia, A., Sestito, P., Villanova, S., et al. 2008, *A&A*, *480*, 79.
Brown, J. A., Wallerstein, G., Geisler, D., & Oke, J. B. 1996, *AJ*, *112*, 1551.
Bukowiecki, L., Maciejewski, G., Konorski, P., et al. 2011, *Acta Astron.*, *61*, 231.
Camargo, D., Bonatto, C., & Bica, E. 2009, *A&A*, *508*, 211.
Camargo, D., Bonatto, C., & Bica, E. 2010, *A&A*, *521*, 42.
Carney, B. 2001, in: *Star Clusters, Saas-Fee Advanced Course 28, Lecture Notes 1998, Swiss Society for Astrophysics and Astronomy*, , eds. L. Labhardt & B. Binggeli, Springer-Verlag (Berlin), 1–222.
Carraro, G., Villanova, S., Monaco, L., et al. 2014, *A&A*, *562*, A39.
Carrera, R. 2012, *A&A*, *544*, A109.
Carrera, R., Gallart, C., Pancino, E., et al. 2007, *AJ*, *134*, 1298.
Carretta, E., Bragaglia, A., Gratton, R. G., et al. 2004, *A&A*, *422*, 951.
Dias, W. S., Alessi, B. S., Moitinho, A., et al. 2012, 2012yCat, VizieR On-line Data Catalog: B/ocl.
Dutra, C. M., Santiago, B. X., & Bica, E. 2002, *A&A*, *383*, 219.
Elson, R. A. W., Fall, S. M., & Freeman, K. C. 1987, *ApJ*, *323*, 54.
Friel, E. D., Jacobson, H. R., & Pilachowski, C. A. 2005, *AJ*, *129*, 272.
Gieles, M., Portegies-Zwart, S., Athanassoula, E., et al. 2006, *MNRAS*, *371*, 793.
Gonzalez, O. A., Rejkuba, M., Zoccali, M., et al. 2012, *A&A*, *543*, 13.
Gratton, R. G., & Contarini, G. 1994, *A&A*, *283*, 911.
Güneş, O., Karataş, Y., & Bonatto, C. 2012, *NA*, *17*, 720.
Jacobson, H. R., Friel, E. D., & Pilachowski, C. A. 2007, *AJ*, *134*, 1216.
Jacobson, H. R., Friel, E. D., & Pilachowski, C. A. 2008, *AJ*, *135*, 2341.
Jacobson, H. R., Pilachowski, C. A., & Friel, E. D. 2011, *AJ*, *142*, 59.
Janes, K. A., & Phelps, R. L. 1994, *AJ*, *108*, 1773.
Kharchenko, N. V., Piskunov, E. A., Schilbach, E., et al. 2013, *A&A*, *558A*, 53.
King, I. 1962, *AJ*, *67*, 471.
King, I. 1966, *AJ*, *71*, 64.
Kroupa, P. 2001, *MNRAS*, *322*, 231.
Lynga, G. 1982, *A&A*, *109*, 213.
Maciejewski, G., & Niedzielski, A. 2007, *A&A*, *467*, 1065.
Mackey, A. D., & Gilmore, G. F. 2003, *MNRAS*, *338*, 120.
Mackey, A. D., Wilkinson, M. I., Davies, M. B., et al. 2008, *MNRAS*, *386*, 65.
Marigo, P., Girardi, L., Bressan, A., et al. 2008, *A&A*, *482*, 883.
Mermilliod, J. C. 1992, *Bull. Inform, CDS*, *40*, 115.
Mermilliod, J.-C., Paunzen, E. 2003, *A&A*, *410*, 51.
Nilakshi, S. R., Pandey, A. K., & Mohan, V. 2002, *A&A*, *383*, 153.
Pasquini, L., Randich, S., Zoccali, M., et al. 2004, *A&A*, *424*, 951.
Piskunov, E. A., Schilbach, E., Kharchenko, N. V., et al. 2008, *A&A*, *477*, 165.
Portegies Zwart, S., & McMillan, S. 2000, *ApJ*, *17*, 2000.
Portegies Zwart, S., Makino, J., McMillan, S., et al. 2002, *ApJ*, *565*, 265.
Portegies Zwart, S., McMillan, S., & Gieles, M. 2010, *ARA&A*, *48*, 431.
Salpeter, E. 1955, *ApJ*, *121*, 161.
Schilbach, E., Kharchenko, N. V., Piskunov, A. E., et al. 2006, *A&A*, *456*, 523.
Schlegel, D. J., Finkbeiner, D. P., & Davis, M. 1998, *ApJ*, *500*, 525.
Sharma, S., Pandey, A. K., Ogura, K., et al. 2006, *AJ*, *132*, 1669.
Skrutskie, M. F., Cutri, R., Stiening, R., et al. 2006, *AJ*, *131*, 1163.
Smiljanic, R., Gauderon, R., North, P., et al. 2008, *A&A*, *502*, 267.
Sollima, A., Carballo-Bello, J. A., Beccari, G., et al. 2010, *MNRAS*, *401*, 577.
Spitzer, L., & Chevalier, R. A. 1973, *ApJ*, *183*, 565.
Tadross, A. L., Werner, P., Osman, A., et al. 2002, *NA*, *7*, 553.
Takahasi, K., & Portegies Zwart, S. F. 2000, *ApJ*, *535*, 759.
Wilson, C. P. 1975, *AJ*, *80*, 175.

SUPPORTING INFORMATION

Additional Supporting Information may be found online in the supporting information tab for this article.

How to cite this article: Günes O, Karatas Y and Bonatto C. A dynamical evolution study of 40 2MASS open clusters. *Astron. Nachr. / AN*. 2017;338:464–488. https://doi.org/10.1002/asna.201712978.